Emergent constraints on the sensitivity of global land surface runoff to temperature based on CMIP6 projections

Yuanfang chai[1], Wouter R. Berghuijs[2], Yao Yue[3], Thomas A.J. Janssen[4], and Han Dolman[4]

[1]Vrije Universiteit Amsterdam
[2]VU Amsterdam
[3]Wuhan university
[4]Vrije Universiteit

November 26, 2022

Abstract

Climate change affects the water cycle. Despite the improved accuracy of simulations of historical temperature, precipitation and runoff in the latest Coupled Model Intercomparison Project Phase 6 (CMIP6), the uncertainty of the future sensitivity of global runoff to temperature remains large. Here, we identify an emergent relationship between the historical sensitivity of precipitation to temperature change (1979–2014) and the future sensitivity of runoff to temperature change (2015–2100), which can be used to constrain future runoff sensitivity estimates. Using this constraint, we estimate that the uncertainties in future sensitivity of runoff have been reduced by 7.2 – 12.0%. The constrained sensitivity of runoff is much larger (36 – 104%) than that directly inferred from original CMIP6 projections. Our constrained sensitivities also indicate more extreme wet conditions and fewer dry conditions. These results suggest that the future global land water cycle is accelerating and comes with more hydroclimatic extremes than previously projected

Title: Emergent constraints on the sensitivity of global land surface runoff to temperature based on CMIP6 projections

Authors: Yuanfang Chai[1], Wouter R. Berghuijs[1], Yue Yao[2], Thomas A.J. Janssen[1] and Han Dolman[1,3*]

[1] Department of Earth Sciences, Free University Amsterdam, Netherlands.

[2] State Key Laboratory of Water Resources and Hydropower Engineering Science, School of Water Resources and Hydropower Engineering, Wuhan University, Wuhan, 430072 China

[3] School of Geography, Nanjing University of Science and Technology, Nanjing, China.

Corresponding author: Han Dolman

Address: Department of Earth Sciences, Free University Amsterdam, Netherlands.

Tel: +31-20-5987358

Email: han.dolman@vu.nl

ORCIDS: http://orcid.org/0000-0003-0099-0457

Key Points:

1. The uncertainty in future runoff sensitivity to temperature have been reduced by 7.2 – 12.0% using the emergent constraint method.

2. Applying an emergent constraint indicates original CMIP6 models underestimated future global runoff sensitivity to temperature by 36 – 104%.

3. Results indicate a shift towards a globally wetter climate.

Abstract: Climate change affects the water cycle. Despite the improved accuracy of simulations of historical temperature, precipitation and runoff in the latest Coupled Model Intercomparison Project Phase 6 (CMIP6), the uncertainty of the future sensitivity of global runoff to temperature remains large. Here, we identify an emergent relationship between the historical sensitivity of precipitation to temperature change (1979 – 2014) and the future sensitivity of runoff to temperature change (2015 – 2100), which can be used to constrain future runoff sensitivity estimates. Using this constraint, we estimate that the uncertainties in future sensitivity of runoff have been reduced by 7.2 – 12.0%. The constrained sensitivity of runoff is much larger (36 – 104%) than that directly inferred from original CMIP6 projections. Our constrained sensitivities also indicate more extreme wet conditions and fewer dry conditions. These results suggest that the future global land water cycle is accelerating and comes with more hydroclimatic extremes than previously projected.

Plain language summary: Climate change can affect river flow, which in turn affects the water availability for society and the environment. However, how much global river flow will change due to rising temperatures remains largely uncertain. A recently introduced methodology (the emergent constraint) can reduce the uncertainties in anticipated future river flow change by using empirical relationships between the current climate and the projected climate. After we apply this method to the latest generation of Earth system models, we substantially reduce the uncertainty of future projections, and the results suggests that land water cycle is accelerating faster and comes with a more extreme wet and fewer extreme dry conditions than previously projected.

Keywords: Emergent constraint; CMIP6; CMIP5; Land surface runoff; Precipitation; Temperature; Climate extremes; Hydrology;

1 Introduction

Land surface runoff is changing with the global climate warming (Labat et al., 2004; Chai et al., 2020). These runoff changes can affect water availability for irrigation, hydropower generation, vegetation growth, industry and human use, especially in arid and semi-arid regions (Sorg et al., 2012). Thus, it is important to provide an accurate estimate of the feedback of future global runoff to rising temperatures. Such knowledge would not only help to better understand the effects of climate change on the terrestrial-water cycle, but could also assist in creating effective decision-making tools for water resources management and environmental protection (Rothausen et al., 2011).

There are however large uncertainties in the future effects of climate on global runoff, largely caused by poor simulation of rainfall and the inaccurate representations of the soil-plant-atmosphere system and human impacts (e.g. dams' operation and irrigation) in current Earth System Models (ESMs) (Du et al., 2016). Such uncertainties are sometimes to the extent that even the sign of the runoff change is unknown (Gedney et al., 2006; Piao et al., 2007; Shi et al., 2011). For the models included in the 5th generation Climate Model Intercomparison Project (CMIP5) (Taylor et al., 2012), the spread of global runoff across these models was rather large, as described in reports of the International Panel on Climate Change and several other studies (IPCC 2014; Alkama et al., 2013; Zhang et al., 2014; Yang et al., 2019). Compared to CMIP 5, the latest generation of ESMs (CMIP6) has increased both the vertical and horizontal spatial resolutions in the models, and includes more comprehensive numerical experimental designs and more detailed processes descriptions. (Meehl et al., 2014; Hall et al., 2019). Yet, the latest generation of ESMs (CMIP6) is still expected to have significant uncertainty in projecting the response of global runoff to a warming climate (Tokarska et al., 2020; Wang et al., 2020).

An evaluation technique — the emergent constraint method (Hall et al., 2006), can reduce the uncertainties of future climate projections, by using strong empirical relationships between current climate and the projected future changes across a range of models (Wenzel et al., 2016, Cox et al., 2013 and 2018; Sherwood et al., 2014;; Eyring et al., 2019; Terhaar et al., 2020; Chai et al., 2021). It thereby offers perspective to also reduce the uncertainties in runoff projections under climate change (Hall et al., 2019). A key challenge in introducing a new emergent constraint is the identification of factor that dominates the uncertainties in global runoff sensitivity, and thereby allows constraining projections of the future climate (Brient et al., 2020). In addition, the empirical relationship would need to be grounded in a physical mechanism we understand (Brient et al., 2020). However, finding such a climate factor can be difficult, because runoff changes in response to warming are affected by many interrelated processes, including atmosphere, soil, and vegetation dynamics (Piao et al., 2007).

In this study, we aim to narrow the large spread of future runoff sensitivities ($\Delta R/\Delta T$) derived from CMIP6 and CMIP5 simulations (Zhang et al., 2014). First, we evaluate the performance of 21 CMIP6 models' simulations of the historical climate by comparing them with both observations (HadCRUT5) and CMIP5 simulations of temperature, precipitation and runoff for the period 1979 – 2014 (See details in SI 1). Subsequently, we assess the uncertainties in future $\Delta R/\Delta T$ during 2015 – 2100 both for CMIP6 models (under climate scenarios SSP126, SSP245, SSP370 and SSP585 (O'Neill et al., 2016)) and for CMIP5 models (under climate scenarios RCP26, RCP45, RCP60 and RCP85 (Taylor et al., 2012)). We use the simulations of precipitation, evaporation, snow melt and soil water content from these earth system model ensembles to infer a main cause of the trends in future $\Delta R/\Delta T$. Identifying such a climate factor would enable to introduce a new emergent constraint reduces the uncertainties of estimated $\Delta R/\Delta T$, under the condition that we find a strong relationship between historical climate changes of the identified variable and future $\Delta R/\Delta T$.

2 Performance of CMIP6 models

2.1 Temperature simulations

The latest generation of CMIP6 models reproduce historical temperatures at both the regional and the global scale better compared to the CMIP5 models (Figs. 1a and b and Fig. S1). CMIP6's performance is weakest in some mountainous regions (e.g. the Himalayas and Andes) and high latitude regions such as eastern Greenland and eastern Siberia (Fig. 1b), but the bias is smaller than in CMIP5 models (Fig. S1). Similar to the previous-generations of ESM ensembles (Rogelj et al., 2012; Keenan et al., 2018), the CMIP6 simulations project widespread warming under various emission scenarios whereby temperatures are rising throughout the 21st century (Fig. 1a and Fig. S2). The highest rates of surface warming are expected at high latitudes, due to polar amplification (Stuecker et a., 2018; Biskaborn et al., 2019). Up to the year 2050, the global warming trends are largely similar across the four emission scenarios (SSP126, SSP245, SSP370 and SSP585), while after 2050 the projected temperatures diverge more clearly between the emission scenarios (Fig. 1a). This divergence is caused by substantially lower CO_2 emissions after 2050 under SSP126 and SSP245 compared to SSP370 and SSP585 (Gidden et al., 2019). Between the periods 2015 – 2024 and 2091 – 2100, the global land surface temperature is estimated to increase by 1.11 ± 0.52 ℃ (i.e. mean ± standard deviation) under SSP126, up to 5.61 ± 1.08 ℃ under SSP585 (Fig. 1a). These reported temperature increases are comparable with those in other studies that also use CMIP6 but with slightly different ensembles (Cook et al., 2020; Fan et al., 2020; Tokarska et al., 2020).

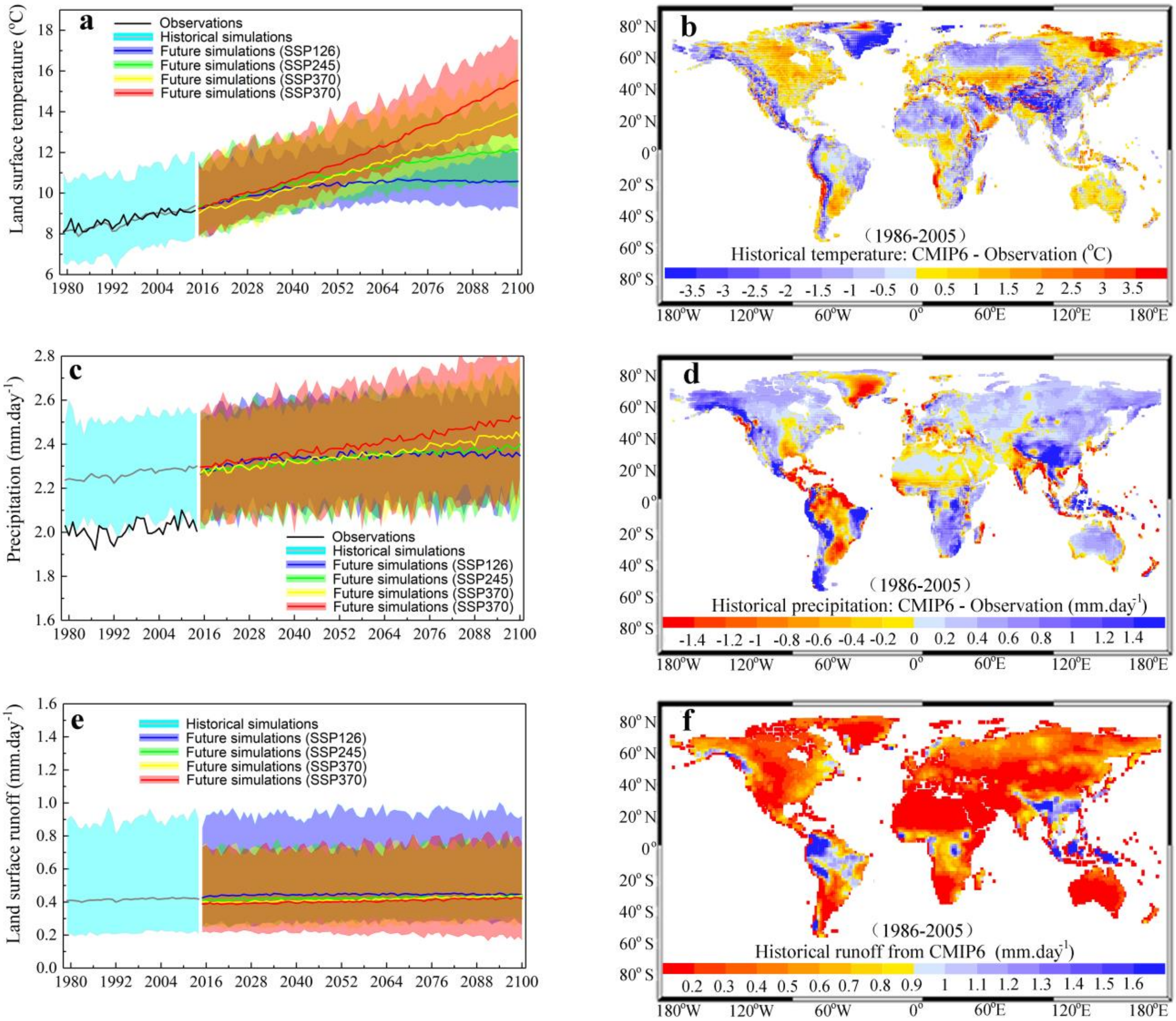

Figure 1. CMIP6 simulations of global temperature (°C), precipitation (mm day^{-1}) and runoff (mm day^{-1}), and their comparison to the HadCRUT5 observational data set and CMIP5 simulations. Panels (**a**), (**c**) and (**e**) show the means and complete ensemble range of simulated trends in global mean temperature, precipitation and runoff based on CMIP6 models during 1979 – 2100 and in observations during 1979 – 2014, respectively. Panels (**b**) and (**d**) show the historical temperature and precipitation of CMIP6 minus the observed temperature and precipitation during 1986 – 2005. Panel (**f**) shows the CMIP6-based global distribution of runoff for the period of 1986 – 2005.

2.2 Precipitation simulations

CMIP6 models simulate historical precipitation better than CMIP5. Noticeable improvements include the reduced underestimation of precipitation in southeastern China, India and South America

(Figs. 1c and d, Fig. S3). However, most CMIP6 models still considerably overestimate global precipitation, whereby overestimations appear especially strong in several mountain regions (e.g. the Himalayas and Andes), but to less extent than in CMIP5 projections (Fig. 1d and Fig. S3). Future global precipitation is predicted to increase, especially in mountain regions, in major monsoon regions, and at high latitudes (Fig. S4). Both these regional and global increases in precipitation are consistent with projections of CMIP5 models (IPCC 2014). CMIP6 predicts future precipitation to reduce mainly in large parts of South America, the Mediterranean, Southern Africa and Oceania, which is also largely consistent with CMIP5. By the end of the 21st century (2091 – 2100), global precipitation is projected to increase by 0.063 ± 0.023 mm day^{-1} (SSP126) up to 0.197 ± 0.065 mm day^{-1} (SSP585) compared to 2015 – 2024.

2.3 Land surface runoff simulations

The CMIP6 historical runoff simulations (Fig. 1f) are significantly lower compared to the observation-based Global Composite Runoff Fields from the Global Runoff Data Centre (Fig. S5) (Fekete et al., 2002), but the underestimation of the global runoff is smaller than for CMIP5 (Fig. S6). Models that are unable to reproduce past climate variations may have biases in their future climate predictions (Klein et al., 2015). Therefore, the underestimation of historical runoff is likely to lead to a underestimation of projections of future runoff. Underestimations of historical runoff are mainly found in humid regions, including eastern North America, Europe, Southeast Asia, Central Africa, and Indonesia. Such biases in modeled global runoff have also been reported in CMIP5 and are likely largely the result of poor descriptions of precipitation, the soil-plant-atmosphere system and human impacts (e.g. dams' operation and irrigation) (Du et al., 2016; Lehner et al., 2019). Global runoff is generally projected to increase over the 21st century (Fig. 1e). The estimated increase in global runoff for the period of 2091 – 2100 compared to 2015 – 2024 ranges from 0.009 ± 0.009 mm day^{-1} (SSP126) up to 0.035 ± 0.032 mm day^{-1} (SSP370), which equates to roughly a 2.25 ± 1.88% to 10.24 ± 10.91% increase. Especially East Asia, Central Africa and high northern latitudes show strong increases in surface runoff over the 21^{st} century (Fig. S7), which is consistent with the projected precipitation increases in these same regions (Fig. S4). In contrast, future land surface runoff is projected to decrease across largely parts of Europe, central North America, Southern Africa, and the Amazon basin.

3 Climate sensitivities

3.1 Global precipitation sensitivity to temperature

CMIP6 models indicate that Earth's warming climate increases global precipitation (Figs. 1a and c). The atmosphere can be expected to reduce its radiative energy under climate warming, which would result in increased longwave emission due to higher temperatures (Previdi et al., 2010). To obey conservation of energy, atmospheric latent heating would increase as an important compensating process, which in turn would increase global precipitation (Liepert et al., 2009). Because of these basic physical mechanisms, we hypothesize that a strong relationship between global precipitation and global land surface temperature will exist. We indeed find a strong linear relationship between precipitation and land surface temperature anomalies ($\Delta P/\Delta T$, mm day^{-1} $°C^{-1}$), both for the historical simulations (r=0.95, p $value$<0.001) as well as the future projections (r≥0.98, p $value$<0.001) (Fig. 2a and Fig. S8). The historical observations also have trends in global precipitation and temperature that are synchronously rising (Fig. 2b). Linear estimates of $\Delta P/\Delta T$ using CMIP6, whether derived from the historical simulations (0.0482 mm day^{-1} $°C^{-1}$, Fig. 2a) or derived from the future projections (0.0343 – 0.0528 mm day^{-1} °C^{-1}) are considerably lower than to the linear estimates of $\Delta P/\Delta T$ derived from the three observational data sets (0.0557 – 0.0612 mm day^{-1} °C^{-1}, Fig. 2c). Precipitation increases are expected to also increase in land surface runoff (e.g., Labat et al., 2004). Therefore, the likely underestimation of $\Delta P/\Delta T$ derived from CMIP6 simulations may also cause an underestimation of $\Delta R/\Delta T$. This potential underestimation of $\Delta R/\Delta T$ is also expected to be present in CMIP5 models, because they yield even lower $\Delta P/\Delta T$ estimates (0.0312 – 0.0550 mm day^{-1} °C^{-1}, Fig. S8) than CMIP6.

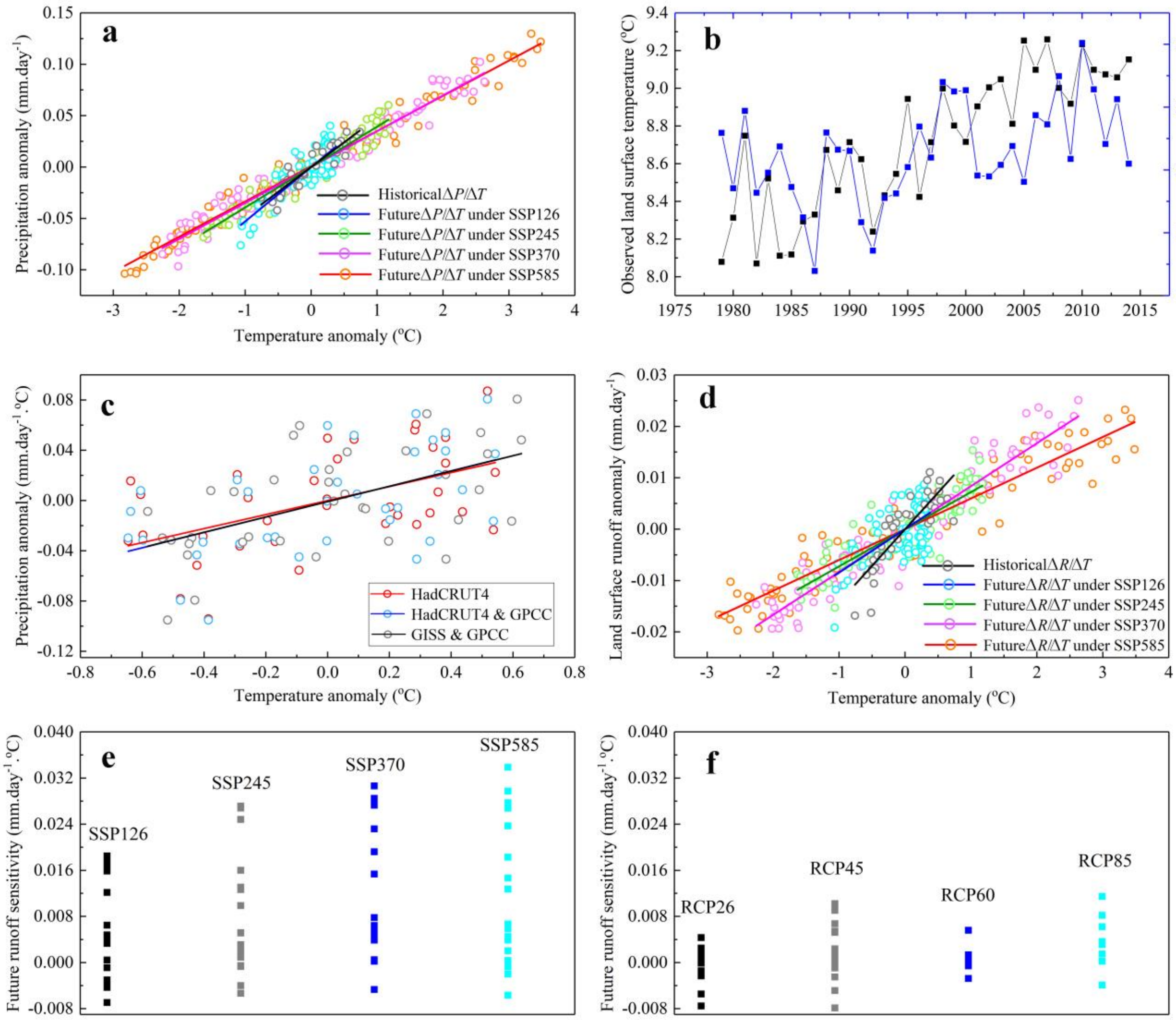

Figure. 2 Estimates of global $\Delta P/\Delta T$ (mm day^{-1} °C^{-1}) and global $\Delta R/\Delta T$ (mm day^{-1} °C^{-1}). Panel (**a**) shows the linear regression relations between annual average daily precipitation and annual average temperature based on CMIP6 outputs for the historical period of 1979 – 2014 (P=0.0482T, r=0.93, p $value$<0.001), and for the future

period of 2015 – 2100 under SSP126 (P=0.0528T, r=0.88, p *value*<0.001), SSP245 (P=0.0393T, r=0.96, p *value*<0.001), SSP370 (P=0.0348T, r=0.98, p *value*<0.001) and SSP585 (P=0.0343T, r=0.99, p *value*<0.001). Panel (**b**) shows the trends in the observed precipitation and temperature during 1979 – 2014 using HadCRUT5 data set. Panel (**c**) shows the observed $\Delta P/\Delta T$ during 1979 – 2014 using HadCRUT5 data set (P=0.0557T, r=0.51, p *value*<0.001), HadCRUT5 – GPCC data set (P=0.0612T, r=0.55, p *value*<0.001) and GISS – GPCC data set (P=0.0609T, r=0.56, p *value*<0.001). Panel (**d**) shows the linear regression relations between runoff and temperature based on CMIP6 outputs for the historical period of 1979 – 2014 (R=0.0142T, r=0.85, p *value*<0.001), and for the future period of 2015 – 2100 under SSP126 (R=0.0085T, r=0.64, p *value*<0.001), SSP245 (R=0.0072T, r=0.88, p *value*<0.001), SSP370 (R=0.0084T, r=0.95, p *value*<0.001) and SSP585 (R=0.0060T, r=0.95, p *value*<0.001). Panels (**e**) and (**f**) show the spread of $\Delta R/\Delta T$ across CMIP6 models and across CMIP5 models, respectively.

3.2 Global runoff sensitivities and their uncertainties

Similar to the above-reported sensitivities of precipitation to temperature changes, we also find a clear sensitivity of global runoff to temperature ($\Delta R/\Delta T$, mm day^{-1} °C^{-1}). This relation is something to be expected because runoff tends to vary systematically with precipitation amounts. CMIP6 outputs exhibit a significant linear relationship between runoff and temperature (Fig. 2d), both in the historical simulations (r=0.85, p *value*<0.001) as well as in the future projections ($0.64 \leq r \leq 0.95$, p *values*<0.001), which corroborates the existence of a distinct global $\Delta R/\Delta T$. Positive relationships between runoff and temperature also exist in CMIP5 models ($0.29 \leq r \leq 0.92$, p *values*<0.001; Fig. S9). Using a similar approach as for the CMIP6 multi-model mean in Fig. 2d, we derived an estimate of future global $\Delta R/\Delta T$ for each individual model (Fig. 2e). As expected, estimated $\Delta R/\Delta T$ relationships show considerable variation across the CMIP6 models, to the extent that both positive and negative sensitivities are estimated for a single emission scenario (Fig. 2e). A wide range of $\Delta R/\Delta T$ relationships are also visible in all RCP scenarios for the 5th generation of CMIP models (Fig. 2f), but with narrower ranges than CMIP6 (possibly due to smaller climate sensitivity ($\Delta T/\Delta CO_2$) in CMIP5 than in CMIP6). It should be noted that across all four emission scenarios the means of estimated $\Delta R/\Delta T$ in CMIP6 (0.005 – 0.011 mm day^{-1} °C^{-1}) are higher than those of CMIP5 (-0.001 –

0.004 mm day^{-1} °C^{-1}). This again suggests that in general, the CMIP6 generation models show a smaller underestimation of the future runoff sensitivity compared to CMIP5.

4 Emergent constraint

4.1 Physical mechanisms

Identifying a dominant climatic factor that drives future runoff changes and its uncertainties is key for increasing the confidence and understanding of the emergent constraint. Once this climatic factor is identified, we can use observations of this climate factor to reduce the uncertainties in estimated $\Delta R/\Delta T$. This is done by combing the empirical relationship between current variability in this climatic factor and the future $\Delta R/\Delta T$ (See *SI 2.1* and *2.2* for details). The water balance dictates that long-term changes in runoff depend on changes in precipitation, snow melt, soil water storage and total evaporation (Lutz et al., 2014; Schoener et al., 2019). The last term, evaporation, is not only driven by near-surface atmospheric conditions, but is also strongly modulated by physiological and structural components of the vegetation (Gedney et al., 2006; Piao et al., 2007). Such complex interacting mechanisms that can affect land surface runoff, might make it difficult to distinguish a single main driving factor.

Through a simple linear regression analysis method we explored the factors contributing to inter-model spread in estimated $\Delta R/\Delta T$ values. Such an approach has been earlier applied to investigate the main drivers behind the changes in seasonal sea-ice albedo feedback (Thackeray et al., 2019). The correlation coefficients of the linear relationships between future global runoff changes and its potential main driving variables (Fig. 3a, and Fig. S10) show that both precipitation and total evaporation exhibit a strong positive relationship with future runoff changes ($0.64 \leq r \leq 0.9$, *p* *value*<0.001). On the contrary, changes in snow melt and soil water storage appear less important as they show much weaker relationships with changes in global runoff ($0.04 \leq r \leq 0.34$, *p values*>0.1) (Fig. 3a). Spatially and temporally varying land surface conditions can make the drivers of regional runoff changes more complex, but on global scale, the effects of precipitation and total evaporation change appear far greater than the other factors. We note that increasing surface air temperatures can be expected to result in a widespread increase in evaporation, which should logically result in a decline of global runoff. However, the future global runoff is predicted to increase in both the CMIP6 and the CMIP5 models. Therefore, we still identify precipitation as the dominant climatic factor affecting changes in runoff that can be used for constraining future $\Delta R/\Delta T$. This constrained relation still holds in the observations of 120 larger rivers as there are significant relations between the observed precipitation and runoff ($r>0.5$ at 68% of the rivers, Fig. 3b), even though these rivers are strongly affected by damming and other human influences (Nilsson et al., 2005). Because changes in precipitation drive runoff changes, and are therefore both are similar in spatial and temporal character, we expect that we can constrain the uncertainties in future $\Delta R/\Delta T$ using the historical $\Delta P/\Delta T$ that we defined above (Fig. 2a).

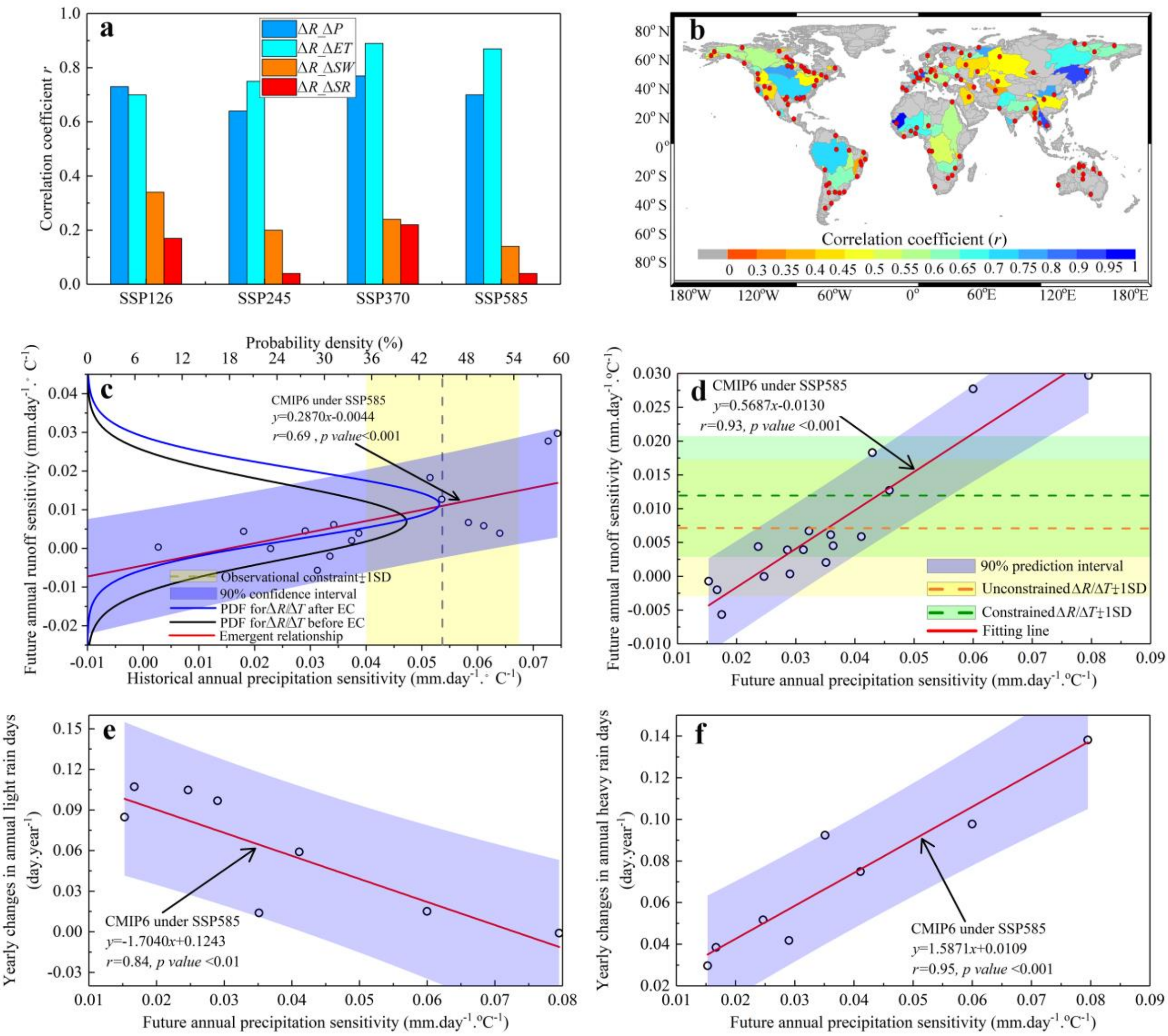

Figure. 3 Emergent constraint on the future global Δ*R*/Δ*T*. Panel (**a**) shows the correlation coefficients *r* for the linear relations between the future runoff changes (Δ*R*) and the future changes in precipitation (Δ*P*), total evaporation (Δ*ET*), soil water content (Δ*SW*) and snow melting runoff (Δ*SR*) respectively, from 2015 – 2024 to 2091 – 2100 based on CMIP6 projections. Panel (**b**) shows correlation coefficients *r* for the linear relations between the observed precipitation and the runoff in the 120 large rivers. Panel (**c**) shows the emergent constraint for the outputs from CMIP6 models under SSP585. Note: red line is the linear relationship between "the future global Δ*R*/Δ*T* during 2015 – 2100 (see left y-axis)" and "the historical global Δ*P*/Δ*T* during 1979 – 2014 (see bottom x-axis)"; yellow shading is the observational Δ*P*/Δ*T* from the HadCRUT5 (0.056 ± 0.016 mm day^{-1} $℃^{-1}$). The blue shading is the 90% prediction error of the linear fitting; the black line and blue line are the probability density functions (PDFs, see top x-axis and left y-axis) for the future global Δ*R*/Δ*T* before and after emergent constraint (*See SI 2.3* for more details); Panel (**d**) is the linear relationship between future Δ*P*/Δ*T* and Δ*R*/Δ*T* under SSP585. Note: The unconstrained and constrained Δ*R*/Δ*T* under SSP585 are 0.007 ± 0.010 mm day^{-1} $℃^{-1}$ and 0.0117 ± 0.0090 mm day^{-1} $℃^{-1}$, respectively. Panels (**e**) and (**f**) are linear relationships between Δ*P*/Δ*T* and future yearly changes in global average annual light rainfall days, and between Δ*P*/Δ*T* and future yearly changes in global average annual heavy rainfall days under SSP585. Note: See detailed trends in global average annual light and

heavy rainfall days in Fig. S11 and Fig. S12, respectively.

4.2 Constrained runoff sensitivity

Despite the relatively large variations in estimates of historical $\Delta P/\Delta T$ and future $\Delta R/\Delta T$ across CMIP6 models (Fig. 2e), we still identify strong linear relationships between them across all emission scenarios ($0.67 \leq r \leq 0.71$, *p values* < 0.001, Fig. 3c for SSP585, and Fig. S13 for SSP126, SSP245 and SSP370). By using the observational $\Delta P/\Delta T$ from the HadCRUT5 dataset (yellow shading in Fig. 3c), we find that most of the CMIP6 climate models lie outside the nominal uncertainty bounds of the observational estimates. This may seem unexpected, but it has been shown that most models do indeed show a systematic bias in their predictions (Klein et al., 2015). This indicates that combining the empirical relationships of historical $\Delta P/\Delta T$ and future $\Delta R/\Delta T$, we can constrain future $\Delta R/\Delta T$, by projecting the observed $\Delta P/\Delta T$ onto the vertical axis (Fig. 3c).

The constrained future $\Delta R/\Delta T$ increases for all emission scenarios (blue line in Fig. 3c and Fig. S13) compared to the original CMIP6 outputs (black line). The original $\Delta R/\Delta T$ ranges from 0.005 ± 0.0082 mm day^{-1}.°C^{-1} (SSP126) up to 0.009 ± 0.0092 mm day^{-1} °C^{-1} (SSP370) (Table S7), whereas the constrained estimates range from 0.0102 ± 0.0075 mm day^{-1} °C^{-1} ^{1} (SSP126) up to 0.0122 ± 0.0081 mm day^{-1} °C^{-1} (SSP370). This increase indicates that the future $\Delta R/\Delta T$ has been underestimated in the multi-model means by 36 – 104% (0.0032 – 0.052 mm day^{-1} °C^{-1}). Such a significant range in underestimation by the CMIP6 original outputs is also present when using the emergent constraint method with the other two observational data sets, where $\Delta R/\Delta T$ is underestimated by 0.0043 – 0.0065 mm day^{-1} °C^{-1} (Fig. S14 and Table S7). Furthermore, the constrained PDF of runoff sensitivity narrows compared to the unconstrained PDFs for all the emission scenarios, which indicates that the inter-model spread in the future $\Delta R/\Delta T$ successfully reduced after the emergent constraint. The reduced uncertainties are 8.5%, 7.2%, 12.0% and 10.0% for the emission scenarios from SSP126 to SSP585 respectively. Similar strong empirical relationships between historical $\Delta P/\Delta T$ and future $\Delta R/\Delta T$ also exist among CMIP5 models under RCP26, RCP45, RCP60 and RCP85 ($0.34 \leq r \leq 0.71$, p *value* < 0.05, Fig. S15), which again increases the estimates of future $\Delta R/\Delta T$ after applying the constraint. These results consistently show that our introduced emergent constraint is valid and can be applied to constrain the models.

By multiplying the future increased multi-model mean temperature (ΔT) by the constrained future $\Delta R/\Delta T$, we estimate the constrained future runoff changes in 2091 – 2100 relative to 2015 – 2024. Future runoff increases estimated using the constrain range from 0.0111 ± 0.0088 mm day^{-1} (SSP126) up to 0.0656 ± 0.0504 mm day^{-1} (SSP585), which is much larger than those of the original future runoff from CMIP6 models which range from 0.009 ± 0.009 mm day^{-1} (SSP126) up to 0.035 ± 0.032 mm day^{-1} (SSP370) (Table S7).

4.3 Implications of the PDF shift

The shift in PDFs of runoff sensitivity indicate that the probabilities of very low runoff sensitivities are much smaller than in the original CMIP6 outputs (Fig. 3c, Fig. S13 and Table S8). The constrained sensitivities indicate it is more likely to be that runoff sensitivities are very high. This suggests that global very wet conditions are more likely, and global very dry conditions more rare. In addition, the future annual $\Delta P/\Delta T$ exhibit a tight positive linear relationship with the future $\Delta R/\Delta T$ for each emissions scenario (Fig. 3d and Fig. S16). This positive relationship, combined with the constrained future $\Delta R/\Delta T$, will shift the $\Delta P/\Delta T$ to a higher value by compared to the unconstrained future $\Delta R/\Delta T$. Both results suggest there may be an underestimation in future $\Delta P/\Delta T$. This again suggest that Earth's land surface may experience globally less dry conditions but more extreme wet conditions in future compared to the original CMIP6 projections.

The expectation of more extreme wet conditions but fewer dry conditions is supported by investigating the relationships between the future $\Delta P/\Delta T$ and the future yearly changes in both global average annual light and heavy rain days (*See SI 2.4*). We find negative relations which indicate that a model with a higher $\Delta P/\Delta T$ has a fewer global average annual light rainfall days (Fig. 3e and Fig. S17). Thus, a potential underestimated $\Delta P/\Delta T$ (Fig. 3d) represents an overestimated frequency in future global average light days. In contrast, future yearly increases in global average annual heavy days exhibit a positive relationship with $\Delta P/\Delta T$ (Fig. 3f and Fig. S18). An underestimated $\Delta P/\Delta T$ moves the future yearly increase the number of global average annual heavy days. Using the constrained future $\Delta R/\Delta T$ from the two other observed data sets (Table S7), we still reach the conclusion that the future increases in global average light rainfall frequency has been overestimated by the CMIP6 models outputs, while that for the global average heavy rainfall frequency has been underestimated.

5 Conclusions

In this study, we find a strong physically-explainable empirical linear relationship between the inter-model spread in the historical global $\Delta P/\Delta T$ and the inter-model spread in the future global $\Delta R/\Delta T$ both for CMIP6 models and for CMIP5 models. This emergent constraint relationship allows us to narrow the spread in future runoff sensitivities estimates from models. The constrained results reveal that sensitivities are much higher than those estimated directly from both the original CMIP6 and CMIP5 outputs. This implies that the land water cycle may be accelerating faster than suggested by the models' initial projections. The constrained estimates also suggest that future global climates will experience less global dry conditions but global more extreme wet conditions compared with the original CMIP6 projections. These implications for climates extremes are also supported by the CMIP6's overestimated future increases in global average annual light rainfall days and CMIP6's underestimated future increases in global average annual heavy rainfall days. We note that this result applies at the averaged global scale and is not necessarily opposed to the "dry regions get drier; wet regions get wetter" theorem that applies to the changes in the regional water cycle. Regional or continental scale feedbacks may still enhance the dryness parts of the globe. However, at the global scale the increased moisture holding capacity of the atmosphere leads to an accelerated hydrological cycle in which the Earth system overall is shifting towards a wetter state of the climate.

References

Alkama, R., Marchand, L., Ribes, A., & Decharme, B. (2013). Detection of global runoff changes: results from observations and CMIP5 experiments. *Hydrology and Earth System Sciences*, **17**(7), 2967. https://doi.org/10.5194/hess-17-2967-2013

Biskaborn, B. K., Smith, S. L., Noetzli, J., Matthes, H., Vieira, G., Streletskiy, D. A., et al. (2019). Permafrost is warming at a global scale. *Nature communications*, **10**(1), 1-11. https://doi.org/10.1038/s41467-018-08240-4

Brient, F. (2020). Reducing uncertainties in climate projections with emergent constraints: Concepts, Examples and Prospects. *Advances in Atmospheric Sciences*, **37**(1), 1-15. https://doi.org/10.1007/s00376-019-9140-8

Chai, Y., Yue, Y., Zhang, L., Miao, C., Borthwick, A.G., Zhu, B., et al. (2020). Homogenization and polarization of the seasonal water discharge of global rivers in response to climatic and anthropogenic effects. *Science of The Total Environment*, **709**, 136062. https://doi.org/10.1016/j.scitotenv.2019.136062

Chai, Y., Martins, G., Nobre, C., Randow, C., Chen, T., & Dolman, H. (2021). Constraining Amazonian land surface temperature sensitivity to precipitation and the probability of forest dieback. *npj Climate Atmospheric Science*, **4**, 6. https://doi.org/10.1038/s41612-021-00162-1

Cook, B. I., Mankin, J. S., Marvel, K., Williams, A. P., Smerdon, J. E., & Anchukaitis, K. J., (2020). Twenty-first century drought projections in the CMIP6 forcing scenarios. *Earth's Future*, **8**(6), e2019EF001461. https://doi.org/10.1029/2019EF001461

Cox, P. M., Pearson, D., Booth, B. B., Friedlingstein, P., Huntingford, C., Jones, C. D., et al. (2013). Sensitivity of tropical carbon to climate change constrained by carbon dioxide variability. *Nature*, **494**(7437), 341-344. https://doi.org/10.1038/nature11882

Cox, P. M., Huntingford, C., & Williamson, M. S. (2018). Emergent constraint on equilibrium climate sensitivity from global temperature variability. *Nature*, **553**(7688), 319-322. https://doi.org/10.1038/nature25450

Du, E., Di Vittorio, A., & Collins, W. D. (2016). Evaluation of hydrologic components of community land model 4 and bias identification. *International journal of applied earth observation and geoinformation*, **48**, 5-16. https://doi.org/10.1016/j.jag.2015.03.013

Eyring, V., Cox, P. M., Flato, G. M., Gleckler, P. J., Abramowitz, G., Caldwell, P., et al. (2019). Taking climate model evaluation to the next level. *Nature Climate Change*, **9**(2), 102-110. https://doi.org/10.1038/s41558-018-0355-y

Fan, X., Duan, Q., Shen, C., Wu, Y., & Xing, C. (2020). Global surface air temperatures in CMIP6: historical performance and future changes. *Environmental Research Letters*, **15**(10), 104056. https://doi.org/10.1088/1748-9326/abb051

Fekete, B. M., Vörösmarty, C. J., & Grabs, W. (2002). High-resolution fields of global runoff combining observed river discharge and simulated water balances. *Global Biogeochemical Cycles*, **16**(3), 15-1. https://doi.org/10.1029/1999GB001254

Gedney, N., Cox, P. M., Betts, R. A., Boucher, O., Huntingford, C., & Stott, P. A. (2006). Detection of a direct carbon dioxide effect in continental river runoff records. *Nature*, **439**(7078), 835-838. https://doi.org/10.1038/nature04504

Gidden, M. J., Riahi, K., Smith, S. J., Fujimori, S., Luderer, G., Kriegler, E., et al. (2019). Global emissions pathways under different socioeconomic scenarios for use in CMIP6: a dataset of harmonized emissions trajectories through the end of the century. *Geoscientific model development*, **12**(4), 1443-1475. https://doi.org/10.5194/gmd-12-1443-2019

Hall, A., & Qu, X. (2006). Using the current seasonal cycle to constrain snow albedo feedback in future climate change. *Geophysical Research Letters*, **33**(3), L03502. https://doi.org/10.1029/2005GL025127

Hall, A., Cox, P., Huntingford, C., & Klein, S. (2019). Progressing emergent constraints on future climate change. *Nature Climate Change*, **9**(4), 269-278. https://doi.org/10.1038/s41558-019-0436-6

IPCC, 2014 Climate change (2014) synthesis report. Contribution of Working Groups I, II and III to the Fifth Assessment Report of the Intergovernmental Panel on Climate Change [Core Writing Team, R.K. Pachauri and L.A. Meyer (eds.)]. IPCC, Geneva, Switzerland

Keenan, T. F., & Riley, W. J. (2018). Greening of the land surface in the world's cold regions consistent with recent warming. *Nature climate change*, **8**(9), 825-828. https://doi.org/10.1038/s41558-018-0258-y

Klein, S. A., & Hall, A. (2015). Emergent constraints for cloud feedbacks. *Current Climate Change Reports*, **1**(4), 276-287. https://doi.org/10.1007/s40641-015-0027-1

Kusunoki, S., & Arakawa, O. (2015). Are CMIP5 models better than CMIP3 models in simulating precipitation over East Asia?. *Journal of Climate*, **28**(14), 5601-5621. https://doi.org/10.1175/JCLI-D-14-00585.1

Labat, D., Goddéris, Y., Probst, J. L., & Guyot, J. L. (2004). Evidence for global runoff increase related to climate warming. *Advances in water resources*, **27**(6), 631-642. https://doi.org/10.1016/j.advwatres.2004.02.020

Lehner, F., Wood, A. W., Vano, J. A., Lawrence, D. M., Clark, M. P., & Mankin, J. S. (2019). The potential to reduce uncertainty in regional runoff projections from climate models. *Nature Climate Change*, **9**(12), 926-933. https://doi.org/10.1038/s41558-019-0639-x

Liepert, B. G., & Previdi, M. (2009). Do models and observations disagree on the rainfall response to global warming?. *Journal of Climate*, **22**(11), 3156-3166. https://doi.org/10.1175/2008JCLI2472.1

Lutz, A. F., Immerzeel, W. W., Shrestha, A. B., & Bierkens, M. F. P. (2014). Consistent increase in High Asia's runoff due to increasing glacier melt and precipitation. *Nature Climate Change*, **4**(7), 587-592. https://doi.org/10.1038/nclimate2237

Meehl, G. A., Moss, R., Taylor, K. E., Eyring, V., Stouffer, R. J., Bony, S., et al. (2014). Climate model intercomparisons: Preparing for the next phase. *Eos, Transactions American Geophysical Union*, **95**(9), 77-78. https://doi.org/10.1002/2014EO090001

Min, S. K., Zhang, X., Zwiers, F. W., & Hegerl, G. C. (2011). Human contribution to more-intense precipitation extremes. *Nature*, **470**(7334), 378-381. https://doi.org/10.1038/nature09763

Neelin, J. D., Sahany, S., Stechmann, S. N., & Bernstein, D. N. (2017). Global warming precipitation accumulation increases above the current-climate cutoff scale. *Proceedings of the National Academy of Sciences*, **114**(6), 1258-1263. https://doi.org/10.1073/pnas.1615333114

Nilsson, C., Reidy, C. A., Dynesius, M., & Revenga, C. (2005). Fragmentation and flow regulation of the world's large river systems. *Science*, **308**(5720), 405-408. https://doi.org/10.1126/science.1107887

O'Neill, B. C., Tebaldi, C., Vuuren, D. P. V., Eyring, V., Friedlingstein, P., Hurtt, G., et al. (2016). The scenario model intercomparison project (ScenarioMIP) for CMIP6. *Geoscientific Model Development*, **9**(9), 3461-3482. https://doi.org/10.5194/gmd-9-3461-2016

Piao, S., Friedlingstein, P., Ciais, P., de Noblet-Ducoudré, N., Labat, D., & Zaehle, S. (2007). Changes in climate and land use have a larger direct impact than rising CO_2 on global river runoff trends. *Proceedings of the National academy of Sciences*, **104**(39), 15242-15247. https://doi.org/10.1073/pnas.0707213104

Previdi, M. (2010). Radiative feedbacks on global precipitation. *Environmental Research Letters*, **5**(2), 025211. http://dx.doi.org/10.1088/1748-9326/5/2/025211

Rothausen, S. G., & Conway, D. (2011). Greenhouse-gas emissions from energy use in the water sector. *Nature Climate Change*, **1**(4), 210-219. https://doi.org/10.1038/nclimate1147

Rogelj, J., Meinshausen, M., & Knutti, R. (2012). Global warming under old and new scenarios using IPCC climate sensitivity range estimates. *Nature climate change*, **2**(4), 248-253. https://doi.org/10.1038/nclimate1385

Schoener, G., & Stone, M. C. (2019). Impact of antecedent soil moisture on runoff from a semiarid catchment. *Journal of Hydrology*, **569**, 627-636. https://doi.org/10.1016/j.jhydrol.2018.12.025

Sherwood, S. C., Bony, S., & Dufresne, J. L. (2014). Spread in model climate sensitivity traced to atmospheric convective mixing. *Nature*, **505**(7481), 37-42. https://doi.org/10.1038/nature12829

Shi, X., Mao, J., Thornton, P. E., Hoffman, F. M., & Post, W. M. (2011). The impact of climate, CO_2, nitrogen deposition and land use change on simulated contemporary global river flow. *Geophysical Research Letters*, **38**(8), L08704. https://doi.org/10.1029/2011GL046773

Sorg, A., Bolch, T., Stoffel, M., Solomina, O., & Beniston, M. (2012). Climate change impacts on glaciers and runoff in Tien Shan (Central Asia). *Nature Climate Change*, **2**(10), 725-731. https://doi.org/10.1038/nclimate1592

Stuecker, M. F., Bitz, C. M., Armour, K. C., Proistosescu, C., Kang, S. M., Xie, S. P., et al. (2018). Polar amplification dominated by local forcing and feedbacks. *Nature Climate Change*, **8**(12), 1076-1081. https://doi.org/10.1038/s41558-018-0339-y

Taylor, K. E., Stouffer, R. J., & Meehl, G. A. (2012). An overview of CMIP5 and the experiment design. *Bulletin of the American meteorological Society*, **93**(4), 485-498. https://doi.org/10.1175/BAMS-D-11-00094.1

Terhaar, J., Kwiatkowski, L., & Bopp, L. (2020). Emergent constraint on Arctic Ocean acidification in the twenty-first century. *Nature*, **582**(7812), 379-383. https://doi.org/10.1038/s41586-020-2360-3

Thackeray, C. W., & Hall, A. (2019). An emergent constraint on future Arctic sea-ice albedo feedback. *Nature Climate Change*, **9**(12), 972-978. https://doi.org/10.1038/s41558-019-0619-1

Tokarska, K. B., Stolpe, M. B., Sippel, S., Fischer, E. M., Smith, C. J., Lehner, F., et al. (2020). Past warming trend constrains future warming in CMIP6 models. *Science Advances*, **6**(12), eaaz9549. https://doi.org/10.1126/sciadv.aaz9549

Wang, Z., Zhan, C., Ning, L., & Guo, H. (2020). Evaluation of global terrestrial evapotranspiration in CMIP6 models. *Theoretical and Applied Climatology*, **143**, 521-531. https://doi.org/10.1007/s00704-020-03437-4

Wenzel, S., Cox, P. M., Eyring, V., & Friedlingstein, P. (2016). Projected land photosynthesis constrained by changes in the seasonal cycle of atmospheric CO_2. *Nature*, **538**(7626), 499-501. https://doi.org/10.1038/nature19772

Yang, Y., Roderick, M. L., Zhang, S., McVicar, T. R., & Donohue, R. J. (2019). Hydrologic implications of vegetation response to elevated CO_2 in climate projections. *Nature Climate Change*, **9**(1), 44-48. https://doi.org/10.1038/s41558-018-0361-0

Yin, L., Fu, R., Shevliakova, E., & Dickinson, R. E. (2013). How well can CMIP5 simulate precipitation and its controlling processes over tropical South America?. *Climate Dynamics*, **41**(11-12), 3127-3143. https://doi.org/10.1007/s00382-012-1582-y

Zhang, X., Tang, Q., Zhang, X., & Lettenmaier, D. P. (2014). Runoff sensitivity to global mean temperature change in the CMIP5 Models. *Geophysical Research Letters*, **41**(15), 5492-5498. https://doi.org/10.1002/2014GL060382

Acknowledgements and Data Availability Statement

AJD and AJJ acknowledge support from the Netherlands Earth System Science Centre Grant/Award Number: 024.002.001. YC acknowledges support from the China Scholarship Council. All the simulated data for this research can be found at https://esgf-node.llnl.gov/projects/cmip6/ (CMIP6) and https://esgf-node.llnl.gov/search/cmip5/ (CMIP5). The observed data of temperature and precipitation from the HadCRUT5 data set can be collected from http://www.cru.uea.ac.uk/. The observation-based Global Composite Runoff Fields and the observed runoff in the 120 large rivers are available at the Global Runoff Data Centre (https://www.bafg.de/GRDC/EN/Home/homepage_node.html).

Author contributions

Yuanfang Chai and Han Dolman led the writing, designed the research and performed the data analysis. Wouter R. Berghuijs, Yao Yue and Thomas A.J. Janssen provided valuable comments and interpretation of results.

Code availability

The code for this study is available by request from the corresponding author.

Competing interests

The authors declare no competing interests.

Additional information

Correspondence and requests for materials should be addressed to Han Dolman.

Title: Emergent constraints on the sensitivity of global land surface runoff to temperature based on CMIP6 projections

Authors: Yuanfang Chai[1], Wouter R. Berghuijs[1], Yue Yao[2], Thomas A.J. Janssen[1] and Han Dolman[1,3*]

[1] Department of Earth Sciences, Free University Amsterdam, Netherlands.

[2] State Key Laboratory of Water Resources and Hydropower Engineering Science, School of Water Resources and Hydropower Engineering, Wuhan University, Wuhan, 430072 China

[3] School of Geography, Nanjing University of Science and Technology, Nanjing, China.

Corresponding author: Han Dolman

Address: Department of Earth Sciences, Free University Amsterdam, Netherlands.

Tel: +31-20-5987358

Email: han.dolman@vu.nl

ORCIDS: http://orcid.org/0000-0003-0099-0457

1. Data

To investigate the performance of CMIP6 models and to estimate the uncertainties in $\Delta R/\Delta T$, we collected monthly temperature, precipitation and land surface runoff from the 21 CMIP6 models (https://esgf-node.llnl.gov/projects/cmip6/, Table S1) both for the historical period (1979 – 2014) and for the future (2015 – 2100) under the emission scenarios of SSP126, SSP245, SSP370 and SSP585 (O'Neill et al., 2016). We collected temperature and precipitation observations from the HadCRUT5 data set (http://www.cru.uea.ac.uk/), and observation-based Global Composite Runoff Fields and observed runoff in the 120 large rivers from the Global Runoff Data Centre (https://www.bafg.de/GRDC/EN/Home/homepage_node.html, Fekete et al., 2002). We collected monthly temperature, precipitation and land surface runoff values of 17 CMIP5 models (Table S2) for the historical period and the future period under the emission scenarios of RCP2.6, RCP4.5, RCP6.0, and RCP8.5 (https://esgf-node.llnl.gov/search/cmip5/, Taylor et al., 2012). We regridded all the CMIP5 and CMIP6 outputs to a common 0.25° × 0.25° latitude-longitude spatial resolution by using nearest neighbor interpolation method for calculating the CMIP6 multi-model mean values.

Poor simulation of other hydrological variables (precipitation, snow melt, soil water content and evaporation) can cause large uncertainties of $\Delta R/\Delta T$ in each CMIP6 models. Therefore, to identify the dominant factor causing spread in the future $\Delta R/\Delta T$ across CMIP6 models through investigating regression relationships of future $\Delta R/\Delta T$ with other hydrological variables, monthly data of precipitation from 21 CMIP6 models, snow melting runoff from 16 CMIP6 models (Table S3), soil water content from 21 CMIP6 models (Table S4) and total evaporation from 19 CMIP6 models (Table S5) under the four emission scenarios of SSP126, SSP245, SSP370 and SSP585 are collected from https://esgf-node.llnl.gov/projects/cmip6/.

To investigate the implications of the constrained $\Delta R/\Delta T$ on extreme rainfall events, the daily data of precipitation from 10 CMIP6 models (Table S6) under the four emission scenarios SSP126, SSP245, SSP370 and SSP585 is also collected from the CMIP6 database. To verify that our main findings are not dependent on a specific observational data set, we also collected the other two data sets, namely "GPCC and HadCRUT5" (https://www.cgd.ucar.edu/cas/catalog/surface/precip/gpcc.html) and the "GISS and GPCC" (https://www.esrl.noaa.gov/psd/data/gridded/data.gistemp.html), used for deriving $\Delta P/\Delta T$ from observations.

2. Methods

2.1 Emergent constraint method

Earth system models are widely used to predict future climate changes at regional to global scale, but these climate projections have large uncertainties (Knutti et al., 2013). The "emergent constraint" method has been developed to reduce such uncertainties (Hall et al., 2006). Specifically, the emergent constraint method consists of a physically-explainable empirical relationship between the inter-model spread of an historical observable variable (namely "independent variable *x*") and the inter-model spread of a future climate predicted variable (namely "dependent variable *y*") (Cox et al., 2018; Chai et al., 2021). The "independent variable *x*" ideally is well enough observed to provide an accurate mean state, variability or variation trend (Klein et al., 2015). By projecting the observed estimate of the "independent variable *x*" with its observational uncertainty (±one standard deviation) onto the y-axis through the empirical linear relationship, a more reliable and accurate "dependent variable *y*" with hopefully narrower uncertainties can be obtained (Brient et al., 2020). Importantly, because empirical relationships could just be fortuitous, a plausible physical mechanism is a fundamental requirement for the underlying empirical relationship (Hall et al., 2019).

2.2 Building an emergent constraint relationship

We use the least-squares linear regression method to build the emergent constraint relationships (Chai et al., 2021). The 'prediction error' of the regression is σ_y, calculated by equation (1); *y(x)* is the linear regression equation (2);

$$\sigma_{y(x)} = s\sqrt{1 + \frac{1}{N} + \frac{(x-\bar{x})^2}{N \cdot \sigma_x^2}} \tag{1}$$

$$y_i = ax_i + b \tag{2}$$

where y_i (future global annual average $\Delta R/\Delta T$) is the value given by x_i (historical observed global annual average $\Delta P/\Delta T$); a and b are the slope and intercept, respectively; s is used for minimizing the least-squares error, calculated by equation (3); and N is the number of data points (number of models). σ_x is the variance of x_i, calculated by equation (4); $\bar{x}$ is the mean value;

$$s^2 = \frac{1}{N-2}\sum_{n=1}^{N}(y - y_i)^2 \tag{3}$$

$$\sigma_x = \sqrt{\sum_{n=1}^{N}(x_i - \bar{x})^2 / N} \tag{4}$$

2.3 Calculation of probability density

Based on the assumption that all model simulations are equally likely and form a Gaussian distribution (Kwiatkowski et al., 2017), we calculate the probability density function (PDF) for the original inter-model spread of the future global annual average $\Delta R/\Delta T$ (y) using equation (5).

$$PDF(y/x) = \frac{1}{\sqrt{2\pi \cdot \sigma_y^2}} \exp\left\{-\frac{(y - f(x))^2}{2\sigma_y^2}\right\} \tag{5}$$

where *PDF(y/x)* is the probability density function around the best-fit linear regression, which represents the estimated probability density of y given x.

We use the equation (6) to calculate the PDF for the constrained future global annual average $\Delta R/\Delta T$ (y). Where *PDF(F/H)* is the probability density of "future global annual average $\Delta R/\Delta T$ (y)" given "historical observable global annual average $\Delta P/\Delta T$ (x)"; *PDF(H)* is the observation-based PDF for "observed global annual average $\Delta P/\Delta T$ (x)"; Thus, after the emergent constraint, the PDF for "the constrained future global annual average $\Delta R/\Delta T$ (y)" (*PDF(F)*) is calculated by numerically integrating *PDF(F/H)* and *PDF(H)*.

$$PDF(F) = \int_{-\infty}^{+\infty} PDF(F/H) \cdot PDF(H) \cdot dH \tag{6}$$

2.4 Definition and calculation of annual heavy and light rain days

Changes in heavy and light rainfall days can directly affect land surface runoff, leading to a tight relationship between these variables. After obtaining the constrained global annual average $\Delta R/\Delta T$, this relationship, combined with the constrained $\Delta R/\Delta T$, is used to investigate the future changes in heavy and light rainfall days, which would be an indication for future changes of global average dry and wet conditions. Extreme light and heavy rainfall days here are defined as the days with rainfall (including days without rainfall) lower than the long-term 10th percentile and the rainfall higher than long-term 90th percentile, respectively. Based on the outputs of the daily precipitation during 2015 – 2100 from 12 CMIP6 models, we estimated the annual light and heavy rainfall days in each grid. The mean value of the annual light and heavy rainfall days in all terrestrial grids is regarded as the global average number of annual drought days and heavy rainfall days.

References

Brient, F. (2020). Reducing uncertainties in climate projections with emergent constraints: Concepts, Examples and Prospects. *Advances in Atmospheric Sciences*, **37**(1), 1-15. https://doi.org/10.1007/s00376-019-9140-8

Chai, Y., Martins, G., Nobre, C., Randow, C., Chen, T., & Dolman, H. (2021). Constraining Amazonian land surface temperature sensitivity to precipitation and the probability of forest dieback. *npj Climate Atmospheric Science*, **4**, 6.

Cox, P. M., Huntingford, C., & Williamson, M. S. (2018). Emergent constraint on equilibrium climate sensitivity from global temperature variability. *Nature*, **553**(7688), 319-322. https://doi.org/10.1038/nature25450

Fekete, B. M., Vörösmarty, C. J., & Grabs, W. (2002). High-resolution fields of global runoff combining observed river discharge and simulated water balances. *Global Biogeochemical Cycles*, **16**(3), 15-1. https://doi.org/10.1029/1999GB001254

Hall, A., & Qu, X. (2006). Using the current seasonal cycle to constrain snow albedo feedback in future climate change. *Geophysical Research Letters*, **33**(3), L03502. https://doi.org/10.1029/2005GL025127

Hall, A., Cox, P., Huntingford, C., & Klein, S. (2019). Progressing emergent constraints on future climate change. *Nature Climate Change*, **9**(4), 269-278. https://doi.org/10.1038/s41558-019-0436-6

Klein, S. A., & Hall, A. (2015). Emergent constraints for cloud feedbacks. *Current Climate Change Reports*, **1**(4), 276-287. https://doi.org/10.1007/s40641-015-0027-1

Kwiatkowski, L., Bopp, L., Aumont, O., Ciais, P., Cox, P. M., Laufkötter, C., et al. (2017). Emergent constraints on projections of declining primary production in the tropical oceans. *Nature Climate Change*, **7**(5), 355-358. https://doi.org/10.1038/nclimate3265

O'Neill, B. C., Tebaldi, C., Vuuren, D. P. V., Eyring, V., Friedlingstein, P., Hurtt, G., et al. (2016). The scenario model intercomparison project (ScenarioMIP) for CMIP6. *Geoscientific Model Development*, **9**(9), 3461-3482. https://doi.org/10.5194/gmd-9-3461-2016

Taylor, K. E., Stouffer, R. J., & Meehl, G. A. (2012). An overview of CMIP5 and the experiment design. *Bulletin of the American meteorological Society*, **93**(4), 485-498. https://doi.org/10.1175/BAMS-D-11-00094.1

Knutti, R., & Sedláček, J. (2013). Robustness and uncertainties in the new CMIP5 climate model projections. *Nature Climate Change*, **3**(4), 369-373. https://doi.org/10.1038/nclimate1716

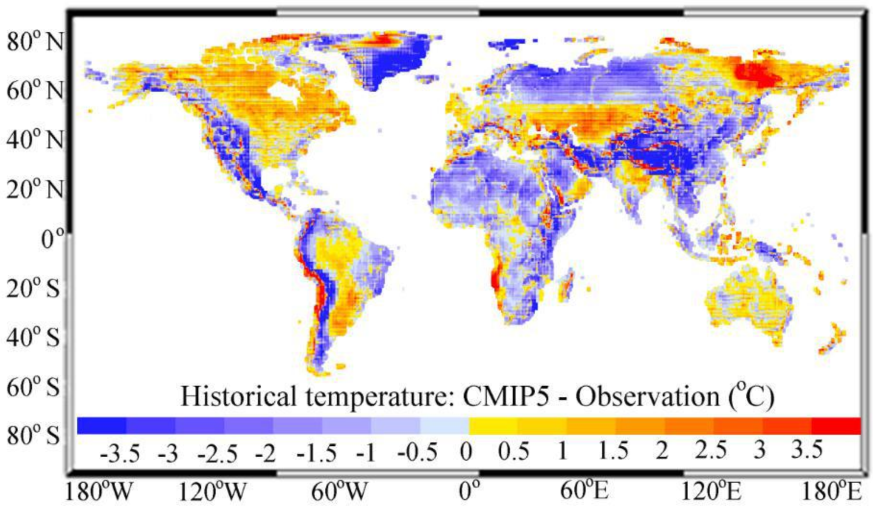

Figure S1. Comparison of CMIP5 simulations of global land surface temperature (℃)to observations from the HadCRUT5 data set. Fig. S1 shows the CMIP5-based difference that is estimated by the simulated historical temperature minus the observed temperature for the period of 1986 – 2005.

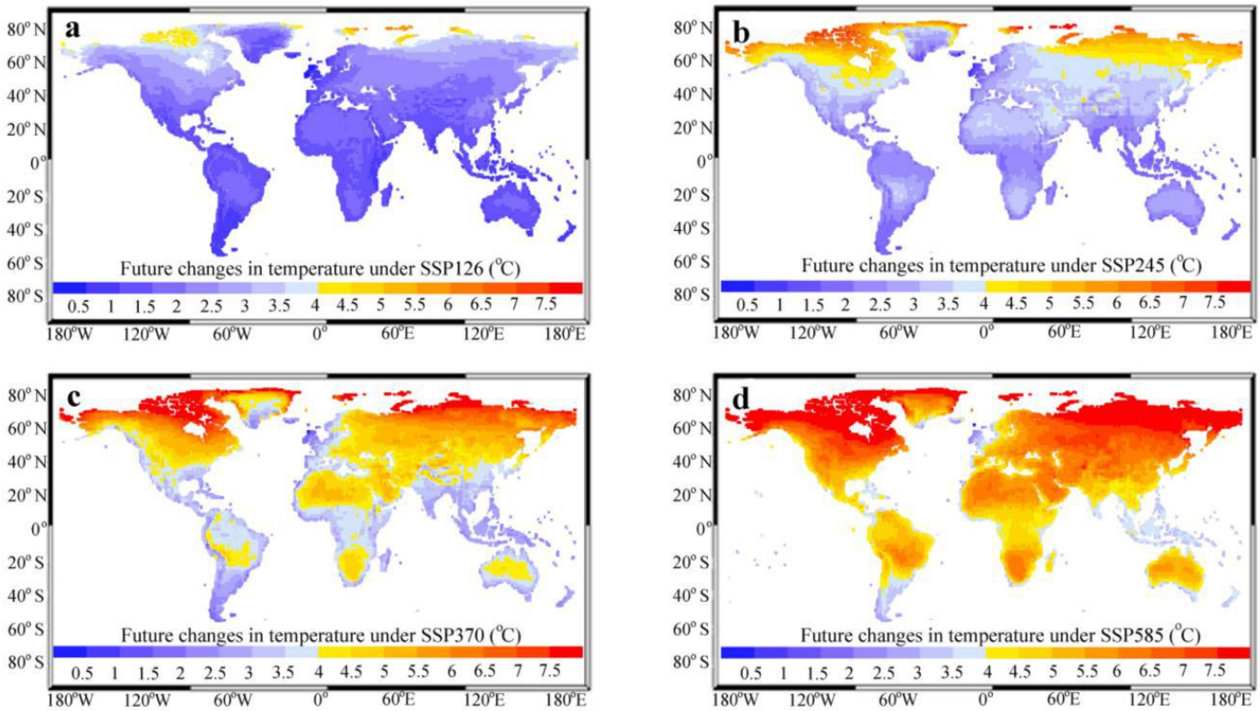

Figure S2. Changes in future land surface temperature based on CMIP6 models. Panels (**a**), (**b**), (**c**) and (**d**) show the CMIP6 multi-model median change in 20-year return values of global annual average land surface temperature as simulated by CMIP6 models in 2081 – 2100 relative to 1986 – 2005 for the emission scenarios of SSP126, SSP245, SSP370 and SSP585, respectively.

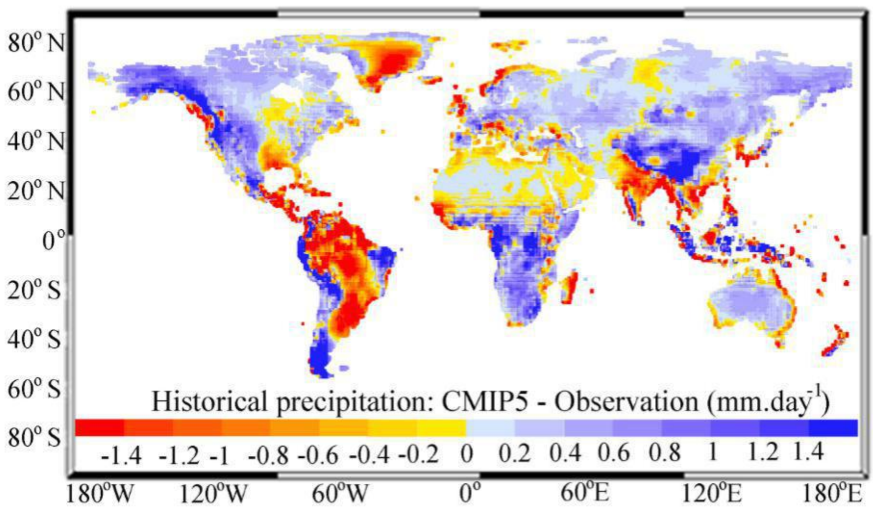

Figure S3. Compariosn of CMIP5 simulations global precipitation (mm day^{-1}) with to observations from the HadCRUT5 data set. Fig. S2 shows the CMIP5-based difference that is estimated by the simulated historical precipitation minus the observed precipitation for the period of 1986 – 2005.

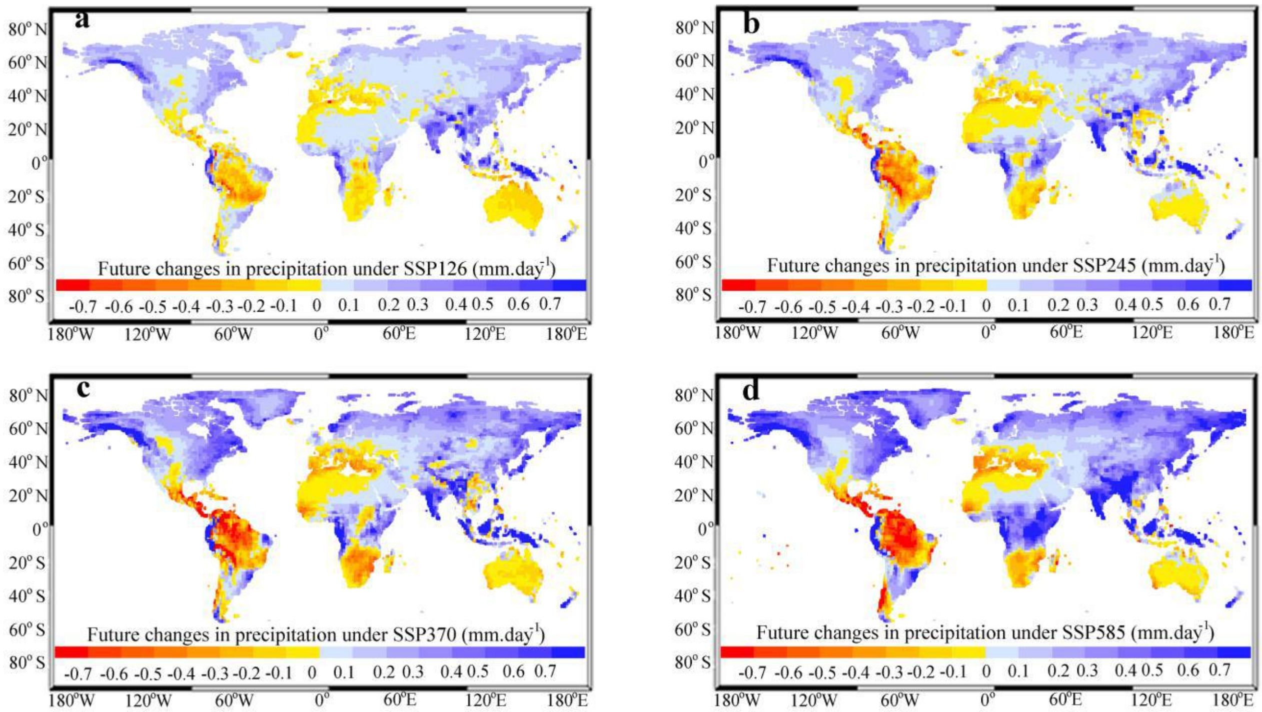

Figure S4. Changes in future precipitation based on CMIP6 models. (**a**), (**b**), (**c**) and (**d**) are the CMIP6 multi-model median change in 20-year return values of global annual average land surface precipitation as simulated by CMIP6 models in 2081 – 2100 relative to 1986 – 2005 for the emission scenarios of SSP126, SSP245, SSP370 and SSP585, respectively.

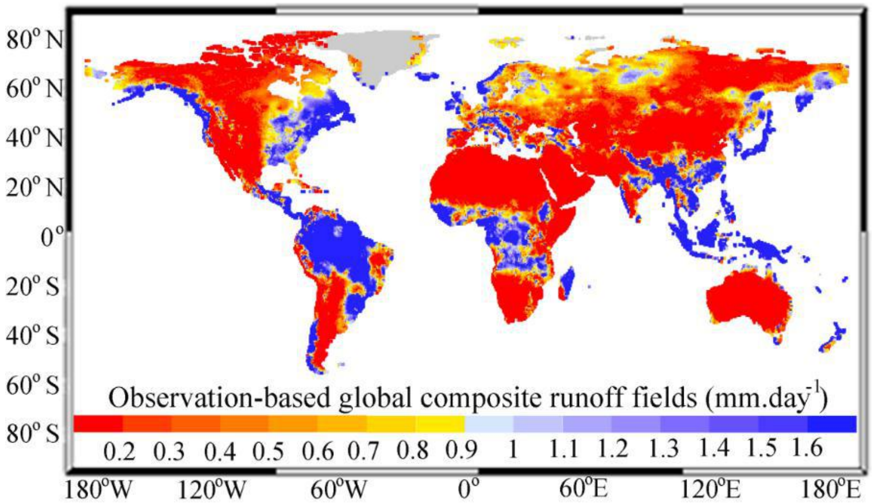

Figure S5. Observation-based Global Composite Runoff Fields from the Global Runoff Data Centre.

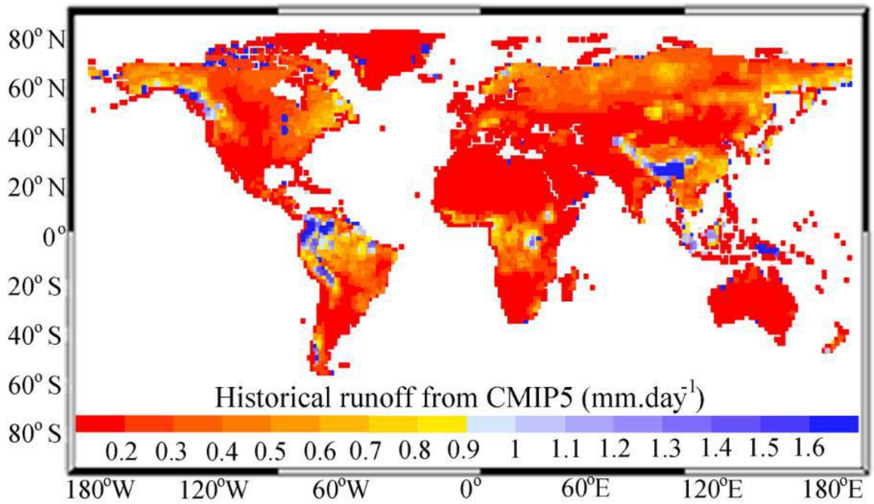

Figure S6. CMIP5-based distribution of the global land surface mean runoff over the period of 1986 – 2005.

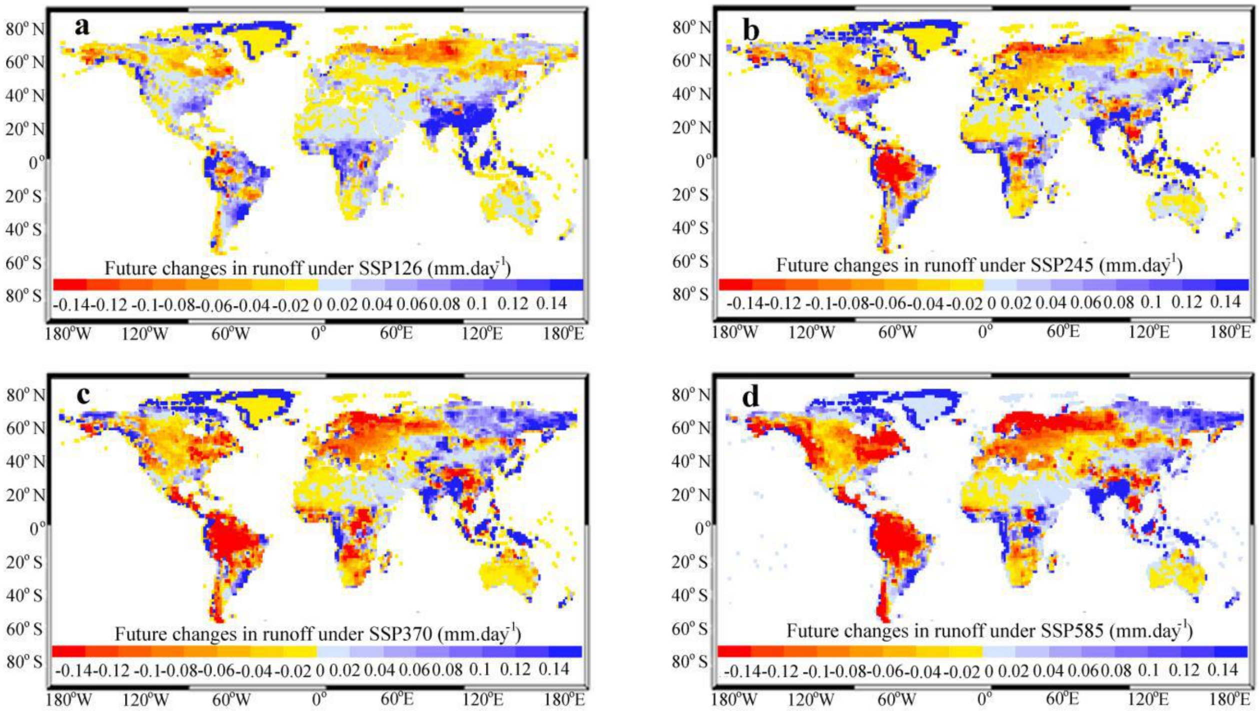

Figure S7. Changes in future land surface runoff based on CMIP6 models. Panels (**a**), (**b**), (**c**) and (**d**) are the CMIP6 multi-model median change in 20-year return values of global annual average land surface runoff as simulated by CMIP6 models in 2081 – 2100 relative to 1986 – 2005 for the emission scenarios of SSP126, SSP245, SSP370 and SSP585, respectively.

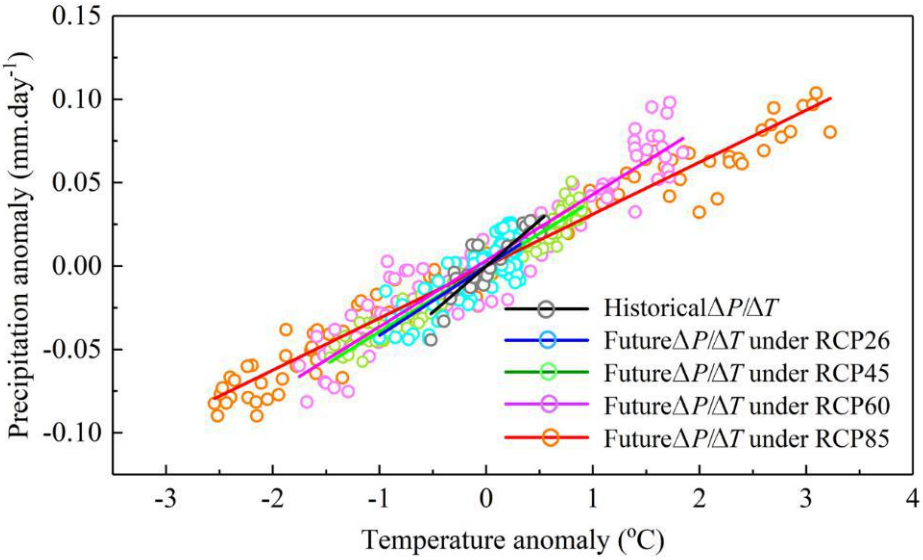

Figure S8. Estimated global $\Delta P/\Delta T$ (mm day^{-1} °C^{-1}) based on CMIP5 model simulations. Fig. S8 shows the linear regression relations between annual average daily precipitation and annual average land surface temperature based on CMIP5 outputs for the historical period of 1979 – 2014 (P=0.0550T, r=0.90, *p value*<0.001), and for the future period of 2015 – 2100 under RCP26 (P=0.0414T, r=0.81, *p value*<0.001), RCP45 (P=0.0392T, r=0.97, *p value*<0.001), RCP60 (P=0.0397T, r=0.95, *p value*<0.001) and RCP85 (P=0.0312T, r=0.98, *p value*<0.001).

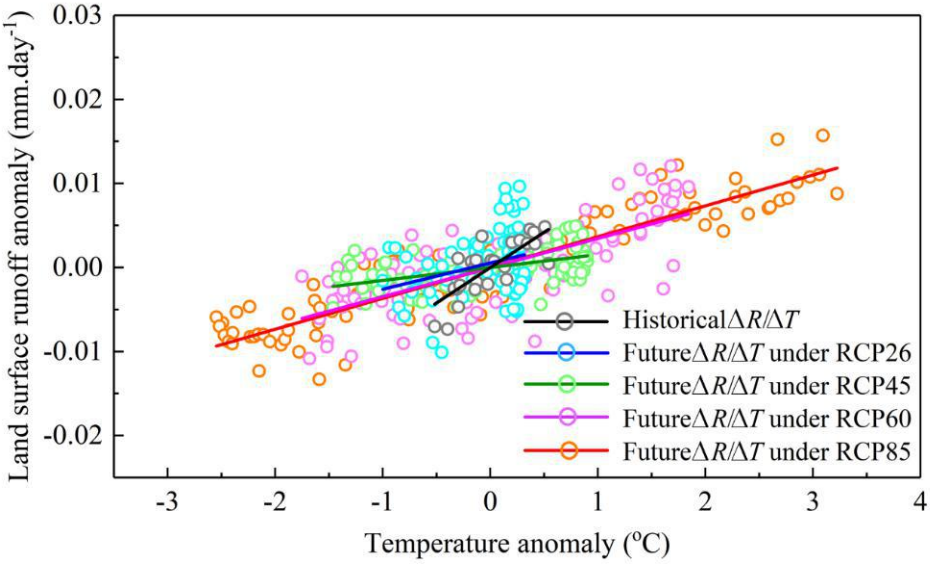

Figure S9. Simulated global $\Delta R/\Delta T$ (mm day^{-1} °C^{-1}) based on CMIP5 models. Fig. S9 shows the linear regression relations between runoff and temperature based on CMIP5 outputs for the historical period of 1979 – 2014 (R=0.0084T, r=0.77, p *value*<0.001), and for the future period of 2015 – 2100 under RCP26 (R=0.0031T, r=0.29, p *value*<0.005), RCP45 (R=0.0015T, r=0.51, p *value*<0.001), RCP60 (R=0.0035T, r=0.70, p *value*<0.001) and RCP85 (R=0.0037T, r=0.92, p *value*<0.001).

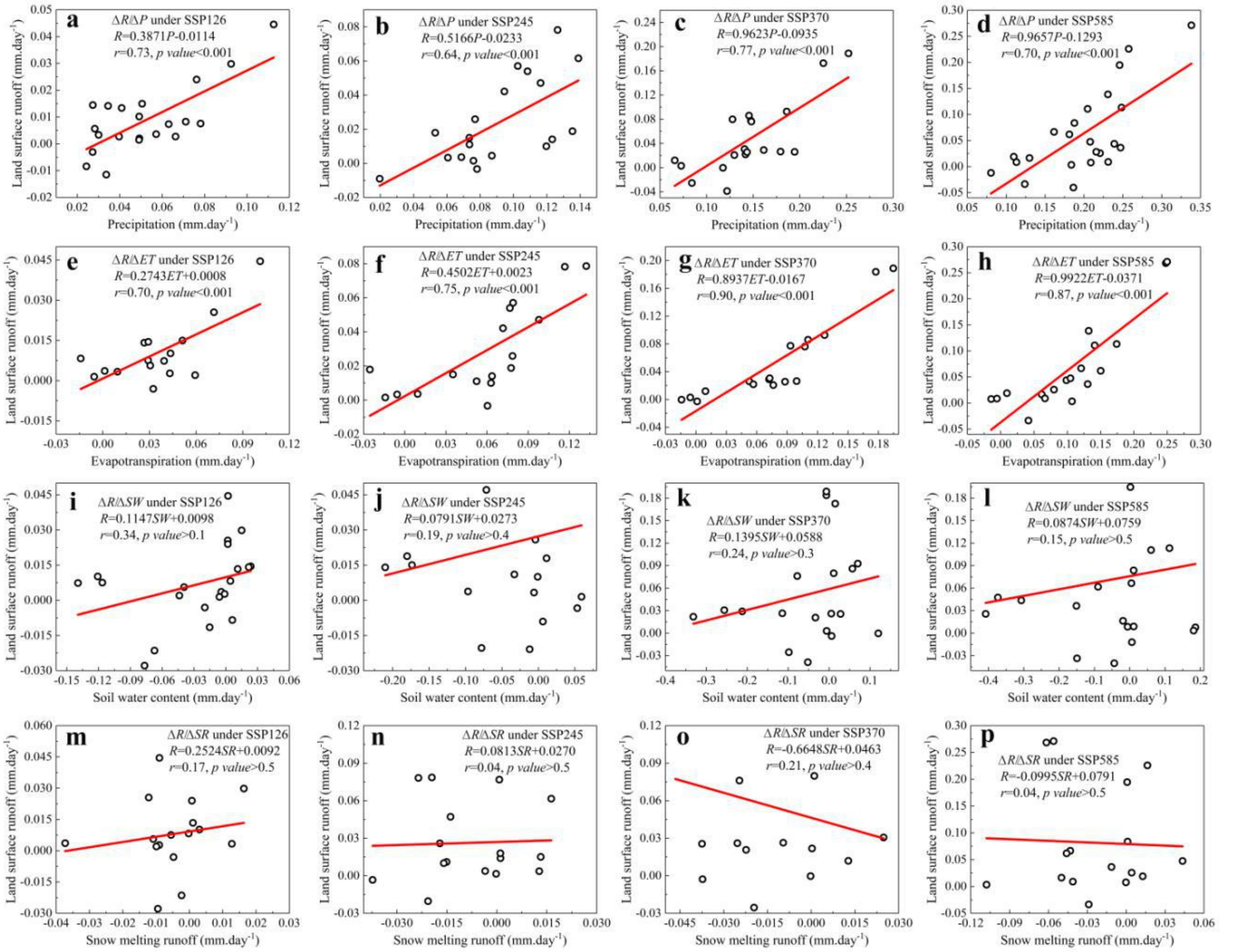

Figure S10. Linear regression relations between the future land surface runoff changes (mm day^{-1}) and the future main climatic factors changes (mm day^{-1}) from 2015–2014 to 2091–2100 based on CMIP6 projections. Panels (**a**), (**b**), (**c**) and (**d**) show the relations between the future land surface runoff changes (ΔR) and the future precipitation changes (ΔP) under SSP126, SSP245, SSP370 and SSP585, respectively. Similarly panels (**e**), (**f**), (**g**) and (**h**) show the relations between the future land surface runoff changes (ΔR) and the future evapotranspiration changes (ΔET). (**i**), (**j**), (**k**) and (**l**) are the relations between the future land surface runoff changes (ΔR) and the future soil water content changes (ΔSW). Panels (**m**), (**n**), (**o**) and (**p**) show the relations between the future land surface runoff changes (ΔR) and the future snow runoff melting runoff changes (ΔSR).

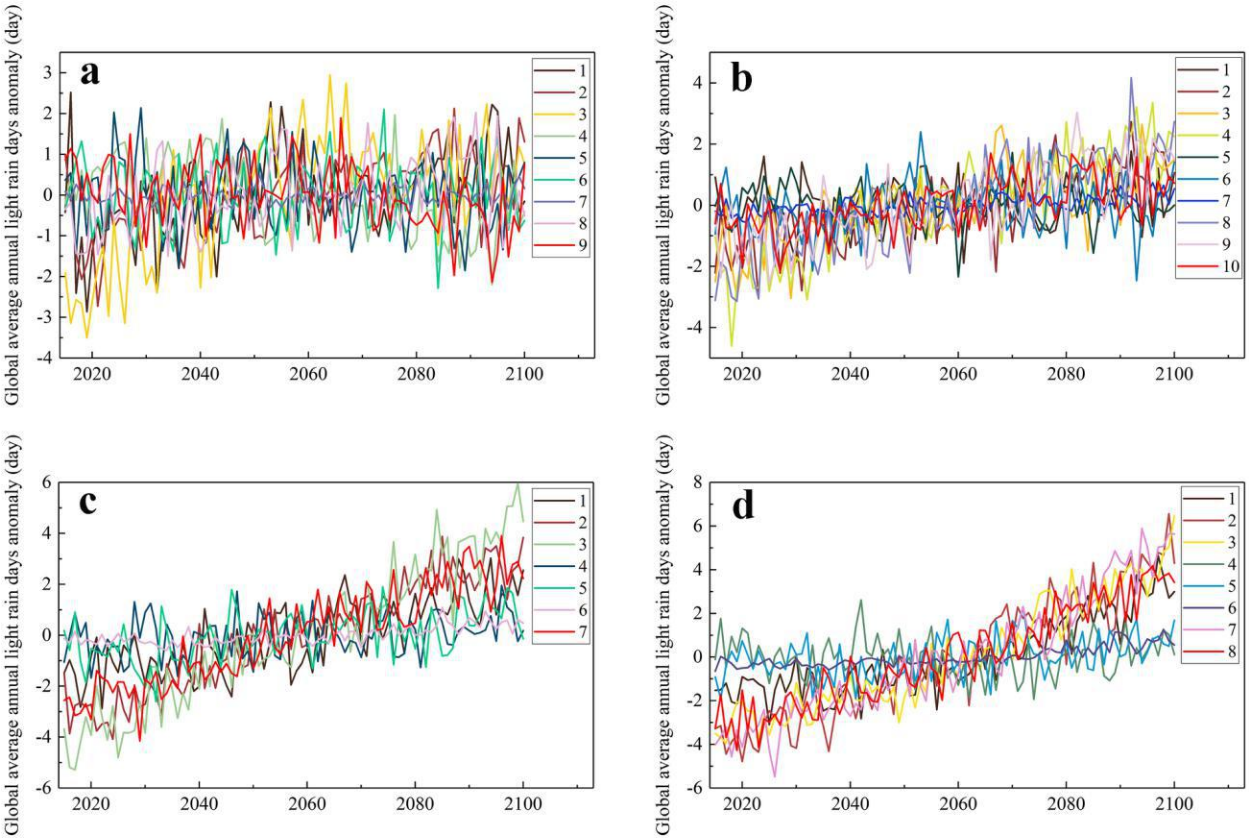

Figure S11. Future changes in global average annual light rain days during 2015-2100 based on the outputs from the 12 CMIP6 models. (a), (b), (c) and (d) are the trends for the emission scenarios under SSP126, SSP245, SSP370 and SSP585, respectively. Each number represents a CMIP6 model (See full name in Table S6)

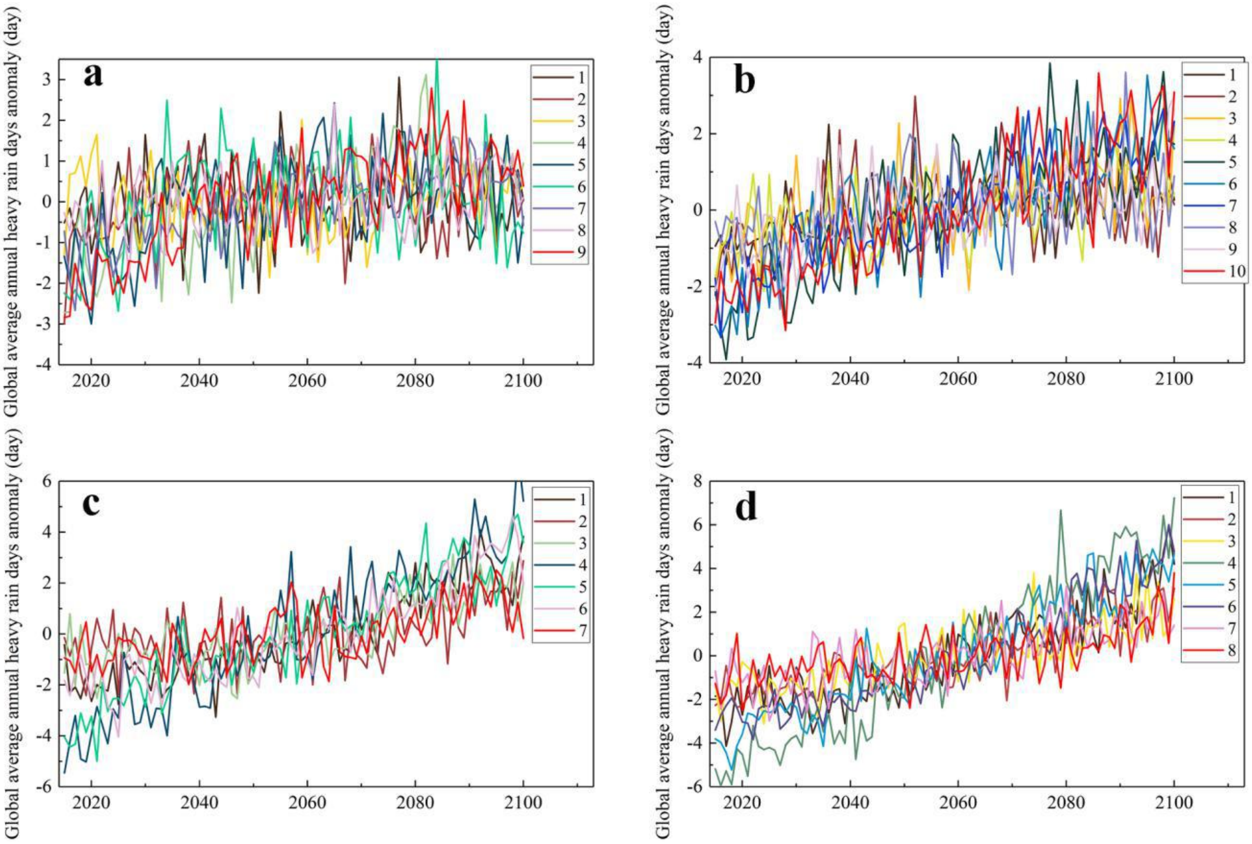

Figure S12. Future changes in global average annual heavy rainfall days during 2015-2100 based on the outputs from the 12 CMIP6 models. Panels (a), (b), (c) and (d) show the trends for the emission scenarios under SSP126, SSP245, SSP370 and SSP585, respectively. Each number represents a CMIP6 model (See full name in Table S6)

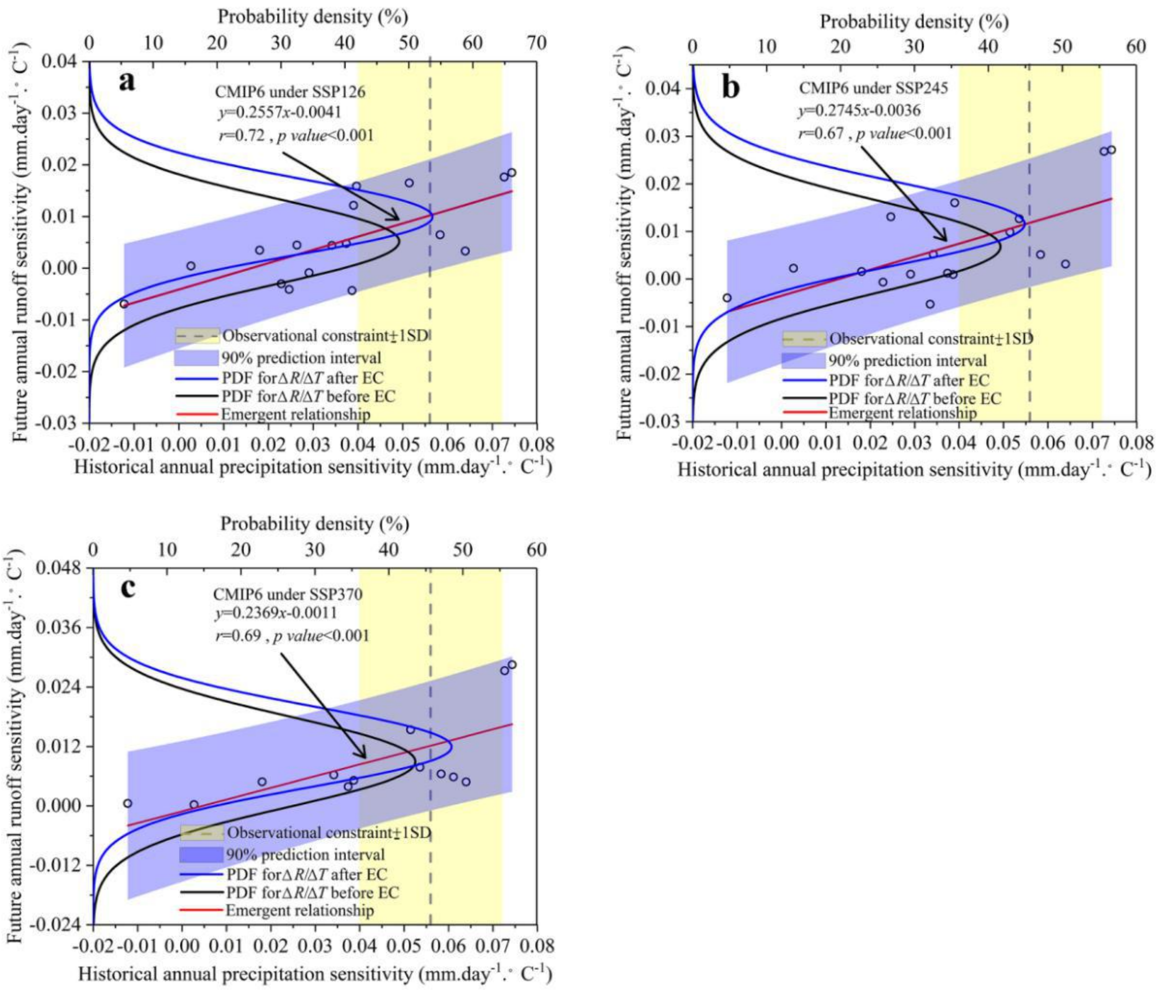

Figure. S13 Emergent constraint on the future sensitivity of global land surface runoff to temperature based on CMIP6 projections. (a), (b) and (c) are the emergent constraint for the outputs from CMIP6 models under SSP126, SSP245 and SSP370 respectively. Note: red line is the linear regression relationship between "the sensitivity of the future global annual land surface runoff to temperature during 2015-2100 (see left y-axis)" and "the sensitivity of the historical global annual precipitation to temperature during 1979-2014 (see bottom x-axis)"; yellow shading is the observational precipitation sensitivity from the HadCRUT5 (observed value ± 1 standard error, 0.056 ± 0.016 mm.day^{-1}.°C^{-1}). The blue shading is the 90% prediction error of the linear fitting; black line and blue line are the probability density functions (PDFs, see top x-axis and left y-axis) for the future global annual runoff sensitivities before and after emergent constraint, by assuming all models are following by Gaussian distribution (*See method for PDF calculation*);

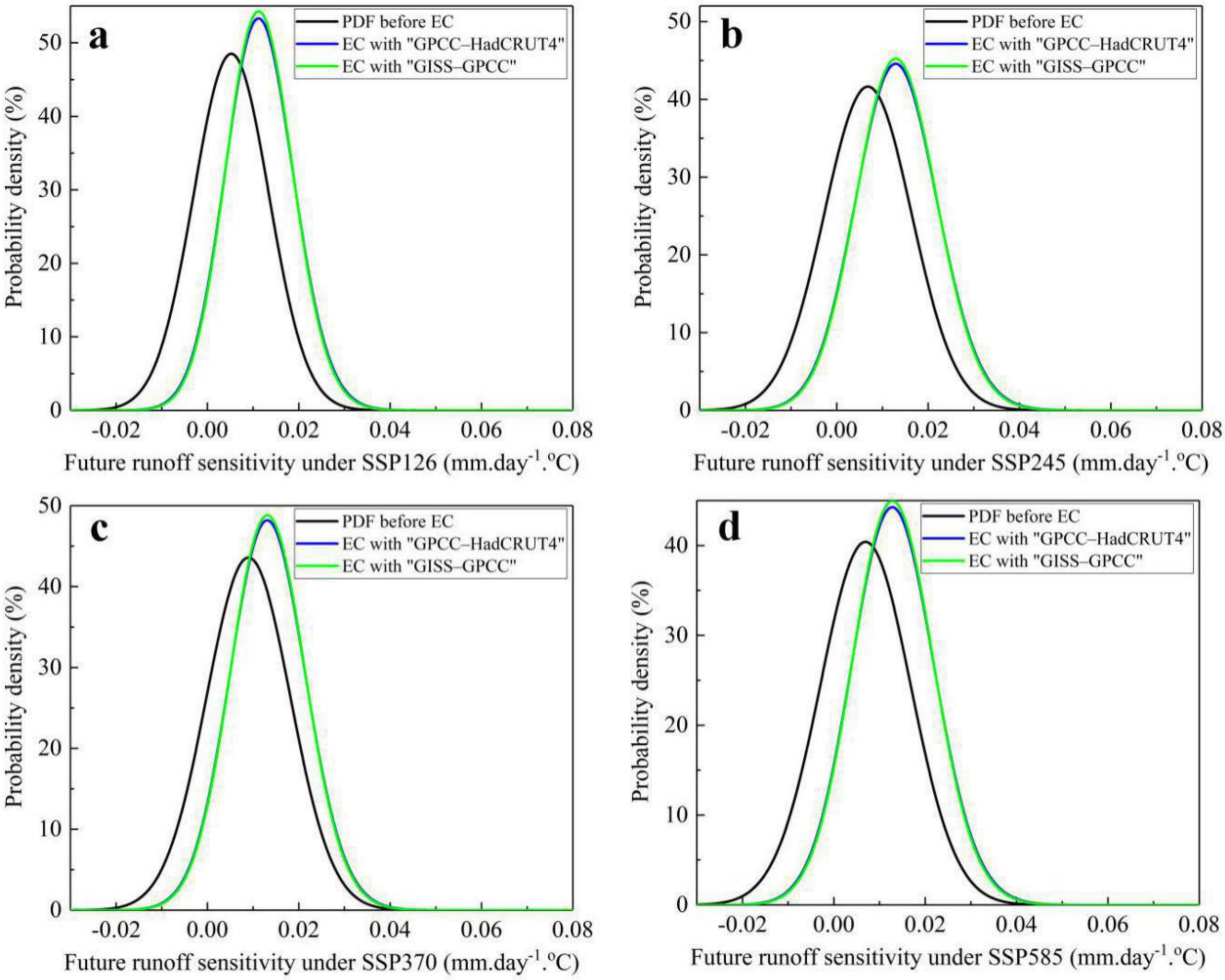

Figure. S14 Emergent constraint (EC) on the future annual runoff sensitivity from CMIP6 projections based on the datasets of "GPCC–HadCRUT5" and "GISS–GPCC". These PDFs are respectively deduced from **a,** the SSP126 scenario, **b,** the SSP245 scenario, **c,** the SSP370 scenario, and **d,** the SSP585 scenario.

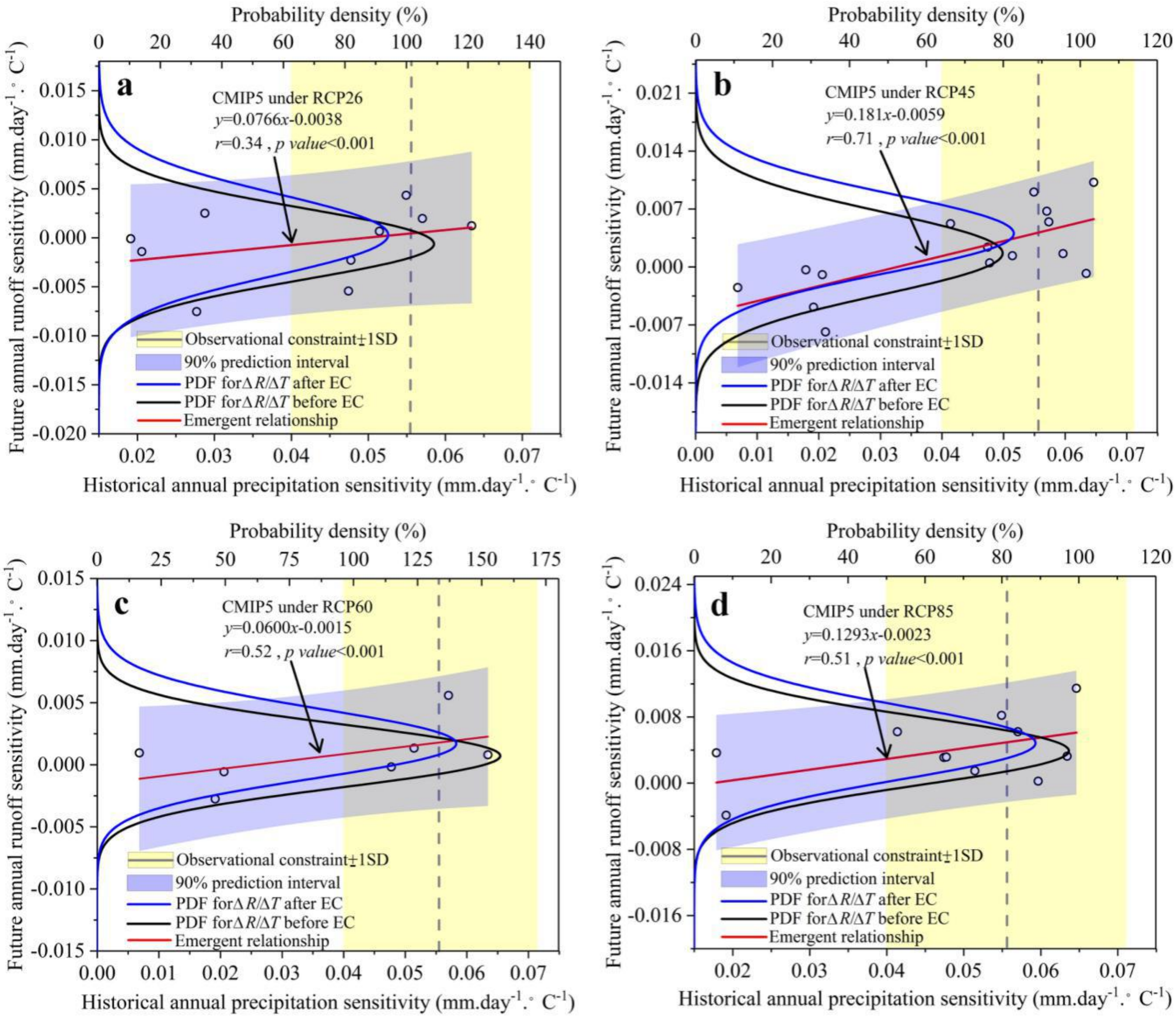

Figure. S15 Emergent constraint on the future sensitivity of global land surface runoff to temperature based on CMIP5 projections. (**a**), (**b**), (**c**) and (**d**) are the emergent constraint for the outputs from CMIP5 models under RCP26, RCP45, RCP60 and RCP85 respectively. Note: red line is the linear regression relationship between "the sensitivity of the future global annual land surface runoff to temperature during 2006-2100 (see left y-axis)" and "the sensitivity of the historical global annual precipitation to temperature during 1979-2005 (see bottom x-axis)"; yellow shading is the observational precipitation sensitivity from the HadCRUT5 (observed value ± 1 standard error). The blue shading is the 90% prediction error of the linear fitting; black line and blue line are the probability density functions (PDFs, see top x-axis and left y-axis) for the future global annual runoff sensitivities before and after emergent constraint, by assuming all models are following by Gaussian distribution;

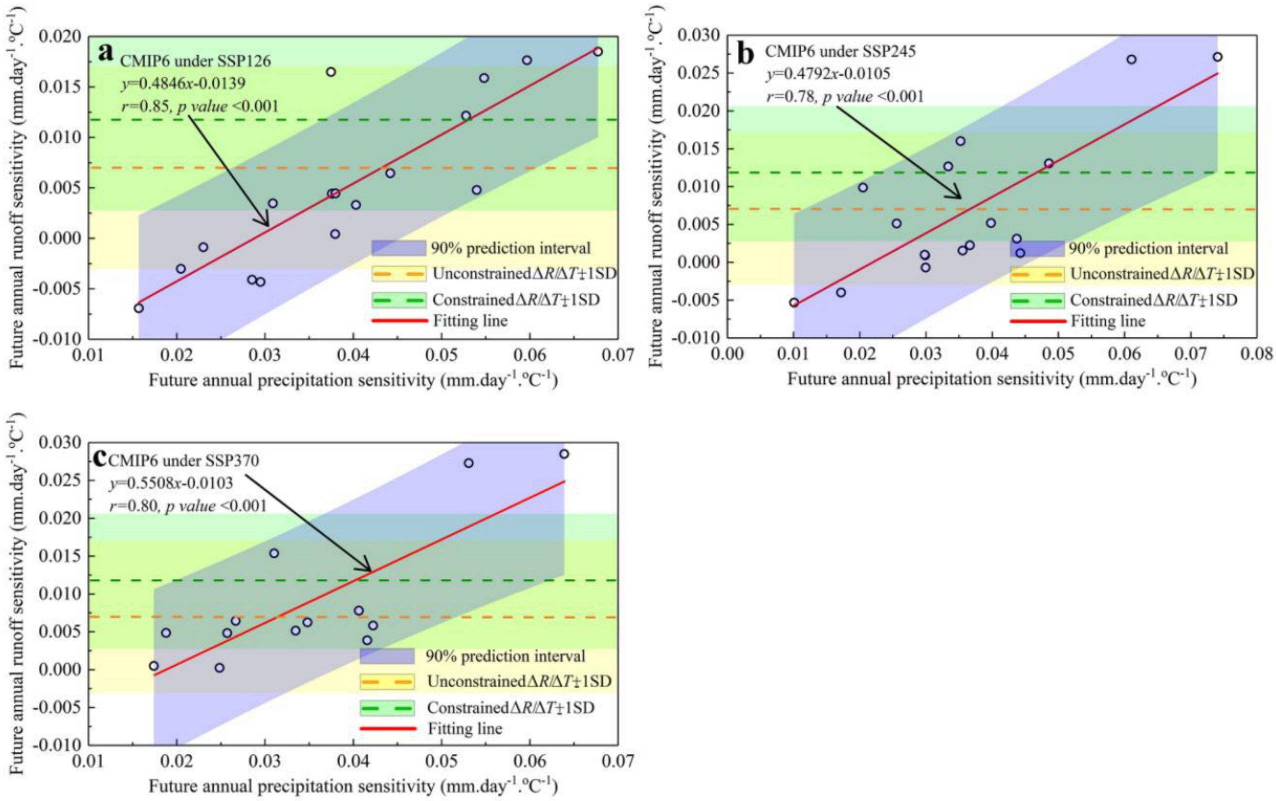

Figure S16. Linear relationships between future annual $\Delta P/\Delta T$ and $\Delta R/\Delta T$ for the CMIP6 models under the emission scenarios of SSP126, SSP245 and SSP370.

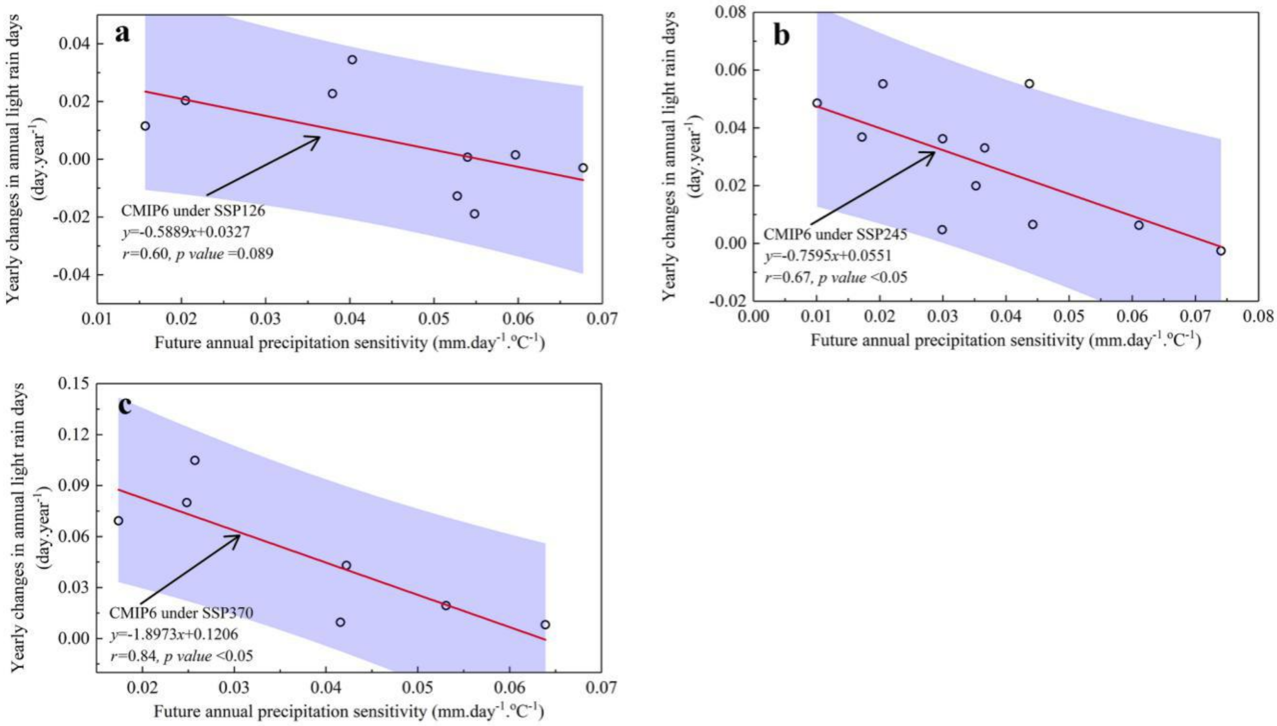

Figure. S17 Constraint on the future yearly changes in global average annual drought days using the constrained future annual runoff sensitivity. Panels (a), (b) and (c) are the constraint for the emission scenarios under SSP126, SSP245 and SSP370, respectively. Note: red line is the linear regression relationship between "future yearly changes in global average annual drought days during 2015-2100 (see left y-axis)" and "the sensitivity of the future global annual runoff to temperature during 2015-2100 (see bottom x-axis)"; yellow shading is the constrained future global annual runoff using the HadCRUT5 (observed value ± 1 standard error, 0.0117 ± 0.009 mm day^{-1} °C^{-1}). The blue shading is the 90% prediction error of the linear fitting; black line and blue line are the probability density functions (PDFs, see top x-axis and left y-axis) for the future yearly changes in global average annual drought days before and after constraint, by assuming all models are following by Gaussian distribution;

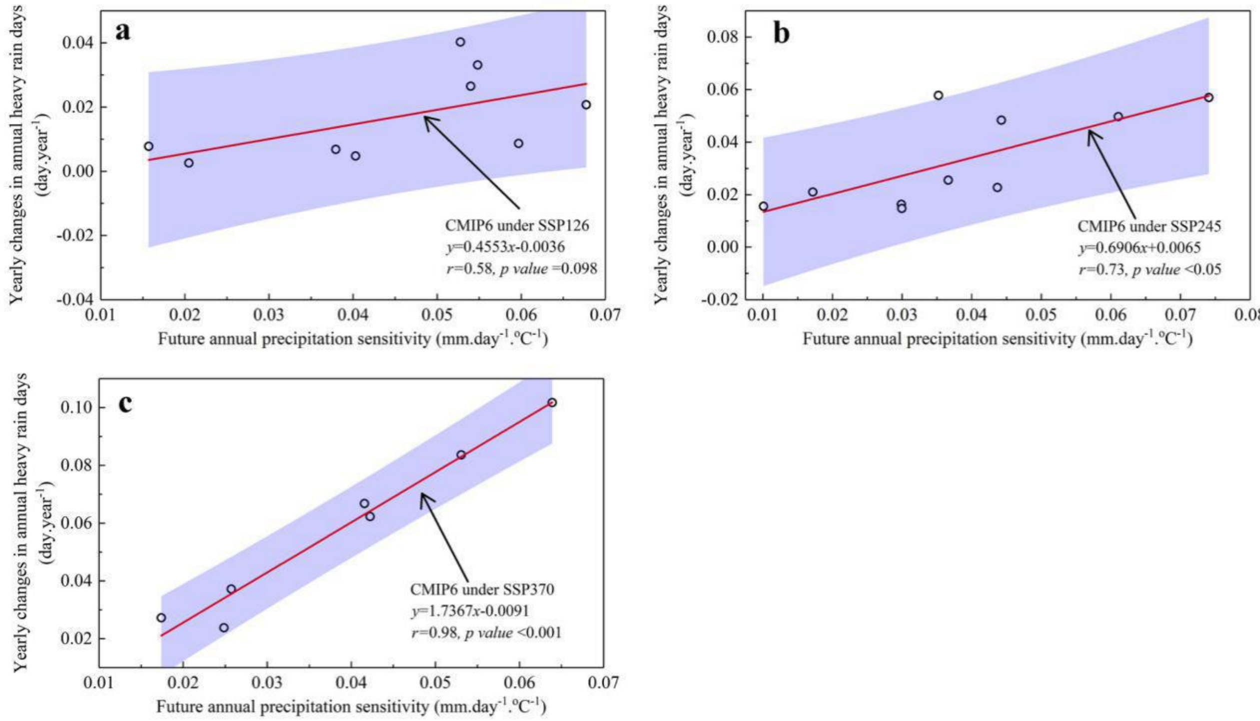

Figure. S18 Constraint on the future yearly changes in global average annual heavy rainfall days using the constrained future annual runoff sensitivity. Panels (a), (b) and (c) are the constraint for the emission scenarios under SSP126, SSP245 and SSP370, respectively. Note: red line is the linear regression relationship between "future yearly changes in global average annual heavy rainfall days during 2015-2100 (see left y-axis)" and "the sensitivity of the future global annual runoff to temperature during 2015-2100 (see bottom x-axis)"; yellow shading is the constrained future global annual runoff using the HadCRUT5 (observed value ± 1 standard error, 0.0117 ± 0.009 mm day^{-1} °C^{-1}). The blue shading is the 90% prediction error of the linear fitting; black line and blue line are the probability density functions (PDFs, see top x-axis and left y-axis) for the future yearly changes in global average annual heavy rainfall days before and after constraint, by assuming all models are following by Gaussian distribution;

Table S1. Full name of the 21 CMIP6 models used for the data of monthly precipitation, runoff and temperature during the historical period (1979–2014) and the future period (2015–2100).

	Precipitation / Runoff / Temperature				
Number	Historical period	Future period under SSP126	Future period under SSP245	Future period under SSP370	Future period under SSP585
1	ACCESS-CM2	BCC-CSM2-MR	BCC-CSM2-MR	ACCESS-CM2	ACCESS-CM2
2	ACCESS-ESM1-5	CESM2	CESM2	BCC-CSM2-MR	ACCESS-ESM1-5
3	BCC-CSM2-MR	CESM2-WACCM	CESM2-WACCM	CESM2	BCC-CSM2-MR
4	CESM2	CNRM-CM6-1	CNRM-CM6-1	CNRM-CM6-1	CESM2
5	CESM2-WACCM	CNRM-CM6-1-HR	CNRM-CM6-1-HR	CNRM-CM6-1-HR	CESM2-WACCM
6	CNRM-CM6-1	CNRM-ESM2-1	CNRM-ESM2-1	CNRM-ESM2-1	CNRM-CM6-1
7	CNRM-CM6-1-HR	FIO-ESM-2-0	FIO-ESM-2-0	GISS-E2-1-G	CNRM-CM6-1-HR
8	CNRM-ESM2-1	GISS-E2-1-G	GISS-E2-1-G	INM-CM4-8	CNRM-ESM2-1
9	FIO-ESM-2-0	HadGEM3-GC31-LL	INM-CM4-8	INM-CM5-0	FIO-ESM-2-0
10	GISS-E2-1-G	INM-CM4-8	INM-CM5-0	IPSL-CM6A-LR	GISS-E2-1-G
11	HadGEM3-GC31-LL	INM-CM5-0	IPSL-CM6A-LR	MIROC6	INM-CM4-8
12	INM-CM4-8	IPSL-CM6A-LR	MIROC6	MPI-ESM1-2-LR	INM-CM5-0
13	INM-CM5-0	MCM-UA-1-0	MIROC-ES2L	NorESM2-MM	IPSL-CM6A-LR
14	IPSL-CM6A-LR	MIROC-ES2L	MPI-ESM1-2-LR		MIROC6
15	MCM-UA-1-0	MPI-ESM1-2-LR	NorESM2-LM		MIROC-ES2L
16	MIROC6	NorESM2-MM	NorESM2-MM		NorESM2-LM
17	MIROC-ES2L	UKESM1-0-LL	UKESM1-0-LL		NorESM2-MM
18	MPI-ESM1-2-LR				
19	NorESM2-LM				
20	NorESM2-MM				
21	UKESM1-0-LL				

Table S2. Full name of the 17 CMIP5 models used for the data of monthly precipitation, runoff and temperature

	Precipitation / Runoff / Temperature				
Number	Historical period	Future period under RCP26	Future period under RCP45	Future period under RCP60	Future period under RCP85
1	ACCESS1-0	CNRM-CM5	ACCESS1-0	CSIRO-Mk3-6-0	ACCESS1-0
2	CNRM-CM5	CSIRO-Mk3-6-0	CNRM-CM5	GISS-E2-R	CNRM-CM5
3	CSIRO-Mk3-6-0	GISS-E2-R	CSIRO-Mk3-6-0	IPSL-CM5A-MR	CSIRO-Mk3-6-0
4	CSIRO-Mk3L-1-2	IPSL-CM5A-MR	CSIRO-Mk3L-1-2	MIROC-ESM	GISS-E2-H-CC
5	GISS-E2-H-CC	MIROC5	GISS-E2-H-CC	MIROC-ESM-CHEM	GISS-E2-R
6	GISS-E2-R	MIROC-ESM	GISS-E2-R	NorESM1-M	inmcm4
7	GISS-E2-R-CC	MIROC-ESM-CHEM	GISS-E2-R-CC	NorESM1-ME	IPSL-CM5A-MR
8	inmcm4	MPI-ESM-LR	inmcm4		IPSL-CM5B-LR
9	IPSL-CM5A-MR	MPI-ESM-MR	IPSL-CM5A-MR		MIROC-ESM
10	IPSL-CM5B-LR	NorESM1-M	IPSL-CM5B-LR		MIROC-ESM-CHEM
11	MIROC5		MIROC-ESM		MPI-ESM-MR
12	MIROC-ESM		MIROC-ESM-CHEM		
13	MIROC-ESM-CHEM		MPI-ESM-MR		
14	MPI-ESM-LR		NorESM1-M		
15	MPI-ESM-MR		NorESM1-ME		
16	NorESM1-M				
17	NorESM1-ME				

Table S3. Full name of the 16 CMIP6 models used for the data of monthly snow melt

	Snow melting runoff				
Number	Historical period	Future period under SSP126	Future period under SSP245	Future period under SSP370	Future period under SSP585
1	ACCESS-CM2	ACCESS-CM2	ACCESS-CM2	ACCESS-CM2	ACCESS-CM2
2	ACCESS-ESM1-5	ACCESS-ESM1-5	ACCESS-ESM1-5	ACCESS-ESM1-5	ACCESS-ESM1-5
3	BCC-CSM2-MR	BCC-CSM2-MR	BCC-CSM2-MR	BCC-CSM2-MR	BCC-CSM2-MR
4	CanESM5	CanESM5	CanESM5	CanESM5	CanESM5
5	CanESM5-CanOE	CanESM5-CanOE	CanESM5-CanOE	CanESM5-CanOE	CanESM5-CanOE
6	CESM2	CESM2	CESM2	CESM2	CESM2
7	CESM2-WACCM	CESM2-WACCM	CESM2-WACCM	CESM2-WACCM	CESM2-WACCM
8	CNRM-CM6-1	CNRM-CM6-1	CNRM-CM6-1	CNRM-CM6-1	CNRM-CM6-1
9	CNRM-ESM2-1	CNRM-ESM2-1	CNRM-ESM2-1	CNRM-ESM2-1	CNRM-ESM2-1
10	GISS-E2-1-G	GISS-E2-1-G	GISS-E2-1-G	GISS-E2-1-G	GISS-E2-1-G
11	HadGEM3-GC31-LL	HadGEM3-GC31-LL	HadGEM3-GC31-LL	IPSL-CM6A-LR	HadGEM3-GC31-LL
12	IPSL-CM6A-LR	IPSL-CM6A-LR	IPSL-CM6A-LR	MIROC6	IPSL-CM6A-LR
13	MIROC6	MIROC6	MIROC6	MIROC-ES2L	MIROC6
14	MIROC-ES2L	MIROC-ES2L	MIROC-ES2L	MPI-ESM1-2-LR	MIROC-ES2L
15	MPI-ESM1-2-LR	MPI-ESM1-2-LR	MPI-ESM1-2-LR	UKESM1-0-LL	MPI-ESM1-2-LR
16	UKESM1-0-LL	UKESM1-0-LL	UKESM1-0-LL		UKESM1-0-LL

Table S4. Full name of the 21 CMIP6 models used for the data of monthly soil water content

Number	Soil water content				
	Historical period	Future period under SSP126	Future period under SSP245	Future period under SSP370	Future period under SSP585
1	ACCESS-CM2	ACCESS-CM2	ACCESS-CM2	ACCESS-CM2	ACCESS-CM2
2	ACCESS-ESM1-5	ACCESS-ESM1-5	ACCESS-ESM1-5	ACCESS-ESM1-5	ACCESS-ESM1-5
3	BCC-CSM2-MR	BCC-CSM2-MR	BCC-CSM2-MR	BCC-CSM2-MR	BCC-CSM2-MR
4	CanESM5	CanESM5	CanESM5	CanESM5	CanESM5
5	CanESM5-CanOE	CanESM5-CanOE	CanESM5-CanOE	CanESM5-CanOE	CanESM5-CanOE
6	CESM2	CESM2	CESM2	CESM2	CESM2
7	CESM2-WACCM	CESM2-WACCM	CESM2-WACCM	CNRM-CM6-1	CESM2-WACCM
8	CNRM-CM6-1	CNRM-CM6-1	CNRM-CM6-1	CNRM-CM6-1-HR	CNRM-CM6-1
9	CNRM-CM6-1-HR	CNRM-CM6-1-HR	CNRM-CM6-1-HR	CNRM-ESM2-1	CNRM-CM6-1-HR
10	CNRM-ESM2-1	CNRM-ESM2-1	CNRM-ESM2-1	INM-CM4-8	CNRM-ESM2-1
11	HadGEM3-GC31-LL	HadGEM3-GC31-LL	HadGEM3-GC31-LL	INM-CM5-0	HadGEM3-GC31-LL
12	INM-CM4-8	INM-CM4-8	INM-CM4-8	IPSL-CM6A-LR	INM-CM4-8
13	INM-CM5-0	INM-CM5-0	INM-CM5-0	MIROC6	INM-CM5-0
14	IPSL-CM6A-LR	IPSL-CM6A-LR	IPSL-CM6A-LR	MIROC-ES2L	IPSL-CM6A-LR
15	MIROC6	MIROC6	MIROC6	MPI-ESM1-2-LR	MIROC6
16	MIROC-ES2L	MIROC-ES2L	MIROC-ES2L	MRI-ESM2-0	MIROC-ES2L
17	MPI-ESM1-2-LR	MPI-ESM1-2-LR	MPI-ESM1-2-LR	NorESM2-LM	MPI-ESM1-2-LR
18	MRI-ESM2-0	MRI-ESM2-0	MRI-ESM2-0	NorESM2-MM	MRI-ESM2-0
19	NorESM2-LM	NorESM2-LM	NorESM2-LM	UKESM1-0-LL	NorESM2-LM
20	NorESM2-MM	NorESM2-MM	NorESM2-MM		NorESM2-MM
21	UKESM1-0-LL	UKESM1-0-LL	UKESM1-0-LL		UKESM1-0-LL

Table S5. Full name of the 19 CMIP6 models used for the data of monthly total evaporation

Number	Total evaporation				
	Historical period	Future period under SSP126	Future period under SSP245	Future period under SSP370	Future period under SSP585
1	ACCESS-CM2	BCC-CSM2-MR	BCC-CSM2-MR	ACCESS-CM2	ACCESS-CM2
2	ACCESS-ESM1-5	CanESM5	CanESM5-CanOE	BCC-CSM2-MR	ACCESS-ESM1-5
3	BCC-CSM2-MR	CanESM5-CanOE	CESM2	CanESM5-CanOE	BCC-CSM2-MR
4	CanESM5	CESM2	CESM2-WACCM	CESM2	CanESM5-CanOE
5	CanESM5-CanOE	CESM2-WACCM	CNRM-CM6-1	CESM2-WACCM	CESM2
6	CESM2	CNRM-CM6-1	CNRM-CM6-1-HR	CNRM-CM6-1	CESM2-WACCM
7	CESM2-WACCM	CNRM-CM6-1-HR	CNRM-ESM2-1	CNRM-CM6-1-HR	CNRM-CM6-1
8	CNRM-CM6-1	CNRM-ESM2-1	GISS-E2-1-G	CNRM-ESM2-1	CNRM-CM6-1-HR
9	CNRM-CM6-1-HR	GISS-E2-1-G	INM-CM4-8	GISS-E2-1-G	CNRM-ESM2-1
10	CNRM-ESM2-1	INM-CM4-8	INM-CM5-0	INM-CM4-8	GISS-E2-1-G
11	GISS-E2-1-G	INM-CM5-0	IPSL-CM6A-LR	INM-CM5-0	INM-CM4-8
12	INM-CM4-8	IPSL-CM6A-LR	MCM-UA-1-0	IPSL-CM6A-LR	INM-CM5-0
13	INM-CM5-0	MCM-UA-1-0	MIROC6	MCM-UA-1-0	IPSL-CM6A-LR
14	IPSL-CM6A-LR	MIROC6	MIROC-ES2L	MIROC6	MCM-UA-1-0
15	MCM-UA-1-0	MIROC-ES2L	MPI-ESM1-2-LR	MIROC-ES2L	MIROC6
16	MIROC6	NorESM2-MM	NorESM2-MM	NorESM2-MM	MIROC-ES2L
17	MIROC-ES2L				NorESM2-MM
18	MPI-ESM1-2-LR				
19	NorESM2-MM				

Table S6. Full name of the 10 CMIP6 models used for the data of daily precipitation

	Daily precipitation			
Number	Future period under SSP126	Future period under SSP245	Future period under SSP370	Future period under SSP585
1	CESM2-WACCM	BCC-CSM2-MR	ACCESS-CM2	ACCESS-CM2
2	CESM2	CESM2-WACCM	CESM2	CESM2-WACCM
3	CNRM-ESM2-1	CESM2	CNRM-ESM2-1	CESM2
4	HadGEM3-GC31-LL	CNRM-ESM2-1	INM-CM4-8	INM-CM4-8
5	INM-CM4-8	INM-CM4-8	INM-CM5-0	INM-CM5-0
6	INM-CM5-0	INM-CM5-0	IPSL-CM6A-LR	IPSL-CM6A-LR
7	IPSL-CM6A-LR	IPSL-CM6A-LR	NorESM2-MM	NorESM2-LM
8	NorESM2-MM	NorESM2-LM		NorESM2-MM
9	UKESM1-0-LL	NorESM2-MM		
10		UKESM1-0-LL		

Table S7. Observed annual precipitation sensitivity ($\Delta P/\Delta T$) ± one standard deviation from the four datasets, and predicted annual land surface runoff sensitivity ($\Delta R/\Delta T$) ± one standard deviation based on CMIP6 models before and after emergent constraint.

	Observed precipitation sensitivity ± one standard deviation (mm day^{-1} °C^{-1})	Emission Scenarios	Future runoff sensitivity before emergent constraint (mm day^{-1} °C^{-1})		Future runoff sensitivity after emergent constraint (mm day^{-1} °C^{-1})		Future original runoff changes ± one standard deviation (mm day^{-1})	Future constrained runoff changes ± one standard deviation (mm day^{-1})
			Mean value	one standard deviation	Mean value	one standard deviation		
HadCRUT5	0.056 ± 0.016	SSP126	0.005	0.0082	0.0102	0.0075	0.009±0.009	0.0111±0.0088
		SSP245	0.007	0.0097	0.0119	0.0090	0.019±0.022	0.0300±0.0225
		SSP370	0.009	0.0092	0.0122	0.0081	0.035±0.032	0.0522±0.0342
		SSP585	0.007	0.0100	0.0117	0.0090	0.032±0.039	0.0656±0.0504
HadCRUT5+GPCC	0.061 ± 0.016	SSP126	0.005	0.0082	0.0115	0.0075	0.009±0.009	0.0122±0.0088
		SSP245	0.007	0.0097	0.0132	0.0090	0.019±0.022	0.0325±0.0225
		SSP370	0.009	0.0092	0.0133	0.0081	0.035±0.032	0.0556±0.0342
		SSP585	0.007	0.0100	0.0131	0.0090	0.032±0.039	0.0729±0.0504
GISS+GPCC	0.061 ± 0.015	SSP126	0.005	0.0082	0.0115	0.0075	0.009±0.009	0.0122±0.0077
		SSP245	0.007	0.0097	0.0132	0.0090	0.019±0.022	0.0325±0.0225
		SSP370	0.009	0.0092	0.0133	0.0080	0.035±0.032	0.0556±0.0342
		SSP585	0.007	0.0100	0.0131	0.0090	0.032±0.039	0.0729±0.0560

Table S8. Implications of the unconstrained and the constrained future runoff sensitivities on the future extreme climates

	SSP126 (mm day^{-1} $°C^{-1}$)		SSP245 (mm day^{-1} $°C^{-1}$)		SSP370 (mm day^{-1} $°C^{-1}$)		SSP585 (mm day^{-1} $°C^{-1}$)	
	<-0.0088	>0.0265	<-0.011	>0.0317	<-0.009	>0.0327	<-0.0114	>0.0325
Unconstrained	5%	0%	3%	0%	2%	0%	3%	0%
Constrained	0%	2%	0%	2%	0%	1%	0%	1%